All-optical polarization-state engineering in quantum cavity optomagnonics

Zhu Liang,[*] Jiahua Li [◉],[†] and Ying Wu[‡]

School of Physics, Huazhong University of Science and Technology, Wuhan 430074, People's Republic of China

We theoretically propose an optical polarization-state engineering based on a cavity optomagnonic platform in the full quantum regime. Here, the optomagnonic interaction can be realized in an yttrium iron garnet (YIG) sphere, which supports both two traveling-photon modes with orthogonal linear polarizations [i.e., horizontally (H-) and vertically (V-) polarized photon modes] and a Kittel magnon mode. In our scheme, the magnons mediate the photons during polarization conversions, and break the time-reversal symmetry in mutual interconversions. Through a triple resonance between the magnon mode, H-polarized, and V-polarized photon modes within the YIG optomagnonic cavity, we demonstrate an all-optical scheme to manipulate the optical polarization behaviors by adjusting an external driving laser, finding that the polarization states of the output light can be well mapped to the whole Poincaré sphere and a large polarization rotation of the output light with photon antibunching and superbunching can be achieved easily for a range of realistic parameters. We find the strong discrepancy in the polarization response between the exact numerical calculation using the full quantum master equation and the semiclassical approximation. In addition, we reveal the magnon-induced broken time-reversal symmetry, which connects the quantum cavity optomagnonics to the classical magneto-optical effect. Our obtained results have potential application in quantum polarization-state engineering, and also offer a further understanding for cavity optomagnonics at the quantum level.

I. INTRODUCTION

The magnons, which are the bosons developed from the collective excitations of spin states via Holstein-Primakoff transformation (see, e.g., Refs. [1–5] and the references therein), have received considerable research interest due to the favorable compatibility with atoms [6–8], photons [9–13], phonons [14,15], polaritons [16,17], and other quanta [18,19]. Additionally, relying on the ultrahigh quality factor (Q) for the quanta and the large spin density, the cavity made of ferromagnetic materials, especially the yttrium iron garnet (YIG) sphere, becomes an important physical model and has motivated extensive investigations [20–27]. Combining the whispering-gallery-mode (WGM) photons and the Kittel-mode magnons inside it, the cavity optomagnonic system supports a three-mode interaction [22–27] and inspires a large amount of novel applications in magnon cooling [28], magnon squeezing [29], magnon laser [30,31], and so on. However, it is notable that all of above works focus on the scalar properties of photons, such as the frequencies and amplitudes of optical fields. Moreover, limited by the weak coupling between the magnons and WGM photons, the semiclassical approach is conventionally adopted to effectively enhance the magnon-photon-photon interaction in the previous studies [22–24,29–31]. Therefore, if the strong-coupling regime of the three-mode optomagnonic interaction can be reached, there are a lot of interests in exploring the vector features and the triple-body

interaction of cavity optomagnonic system in the quantum regime.

On the other hand, arbitrary manipulation and conversion of quantum states of photons is a crucial challenge towards the applications in quantum information and photonic networks today. It has attracted much attention in the related fields, such as condensed matter optics [32–34] and quantum optics [35–38], etc. A standard paradigm in quantum state transfer is the "beam-splitter" form, which is an optimal assumption for quantum state transfer between the motion and the light [39–43]. This kind of semiclassical method can overcome the weak light-matter coupling, in which the effectively enhanced linear coupling is proportional to the steady-state cavity amplitude [44,45]. Nevertheless, both the phase noise and the quantum fluctuation are omitted, which are important in a full quantum system. Recently, a polarization conversion has been proposed and proved in some works in the cavity–quantum-dot (QD) system [46,47]. Due to the strong coupling between the atom and the photon, together with the atom-induced phase shift on the incident photon [48], optical polarization-state transfer can be analyzed and achieved in the cavity-QD system in the quantum approach. In the magnetically biased materials, as everyone knows, that the polarization of the traveling light rotates inside the solid block [49–52]. It is shown that the phase of traveling light can be changed during propagation in the material. In other words, the magnons can also induce phase shift on the input photons. Furthermore, an alternative scheme has been recently proposed and it is shown that an ultrastrong optomagnonic coupling can be obtained in the epsilon-near-zero (ENZ) regime [53,54], which offers some prospects for looking at polarization-state conversion in cavity optomagnonic system, or other deeper studies in quantum cavity optomagnonics.

―――――――
[*]zhuliang955@163.com

[†]Author to whom correspondence should be addressed: huajia_li@163.com
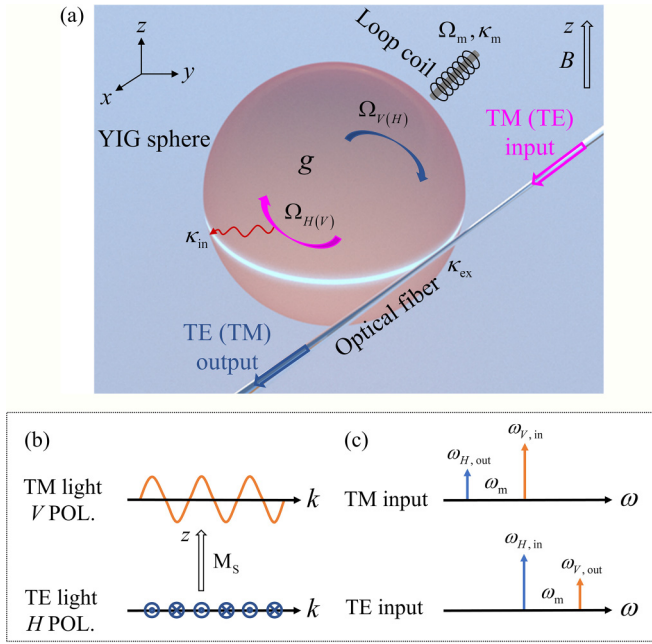
[‡]yingwu2@126.com

FIG. 1. (a) Schematic illustration of cavity optomagnonic system under an externally applied static magnetic field. Two optical WGMs $\hat{a}_V$ and $\hat{a}_H$ for photons are coupled to a magnetostatic mode $\hat{m}$, called a Kittel mode for magnons via the optomagnonic interaction. Each mode can be individually driven externally, in order to realize the polarization-state conversion. For example, the photon WGMs of the YIG sphere can be addressed with an optical nanofiber and the Kittel magnon mode can be excited with a microwave field from a network analyzer via a loop coil near the YIG sphere [22,25]. The output signals in various polarization bases can be analyzed by the polarization tomography technique [47]. (b) TM and TE fields together with the corresponding polarization states, distinguished by their electric components. The orange line represents the sine wave of the electric component of a TM light. The blue marks depict the antinodes of the electric field of a TE light. The wave vectors k along the x axis are perpendicular to the saturation value of the magnetization M_s along the z axis, which corresponds to the Voigt configuration. The electric field of the TM light oscillates parallel to M_s, which is defined as the V polarization (abbreviated as V POL). The electric field of the TE light oscillates perpendicular to M_s, i.e., the H polarization (abbreviated as H POL). (c) The down-conversion of the TM input laser (upper) and the up-conversion of the TE input laser (lower), respectively. The physical meaning of the other used notations is described in the text.

Motivated by these developments mentioned above [46,47,53,54], in this work we explore the polarization dynamics of a quantum cavity optomagnonic system (see Fig. 1 below) and propose a magnon-medium polarization-state conversion inside an YIG sphere with sub-mm radii. Physically, as a distinctive feature of the magnetized YIG materials, the Brillouin scattering (BLS) can bring the geometric birefringence and split the degenerate photons into different WGMs and different polarization states inside the YIG sphere [22–26]. In view of this BLS, the transverse electric (TE) field and transverse magnetic (TM) field can propagate in the spherical cavity with different WGMs, and both the polarization state and the wavelength of WGM photons can be converted by eliminating or creating the Kittel-mode

magnons. Based on such a physical picture, here we focus mainly on the polarization-state conversion properties of input and output light, to the best of our knowledge, which is rarely studied in the full quantum regime by taking advantage of the coupling between two orthogonally polarized photon modes and a magnon mode inside an optomagnonic cavity.

To begin with, we present the system Hamiltonian which governs the two transition channels of photons in WGMs: (i) A V-polarized photon is Brillouin scattered into an H-polarized photon by creating a magnon in the Kittel mode and (ii) an H-polarized photon is Brillouin scattered into a V-polarized photon by eliminating a magnon in the Kittel mode, respectively. Compared with the semiclassical approach in the previous studies [38–42], in which a strong optical control field and a pump signal are required without the consideration of quantum fluctuation (incoherence) of the system, here we only apply a weak optical driving laser and a weak magnonic microwave drive and include all the quantum fluctuation. In order to generate different polarized output photons, the incident polarization angle of the applied driving field is rotated. By making use of the optomagnonic Hamiltonian of the driven system, we solve the Lindblad master equation with numerical simulations to obtain the density matrix of the whole system in the steady-state limit. For confirming the appearance of the polarization-state conversion, we evaluate the average photon numbers of the H and V polarizations inside the YIG sphere cavity.

Then, resorting to the input-output formalism, the statistics of the output photons after the conversion can be calculated. It is found that the dip (the minimum value) of the second-order correlation function $g_{ij}^{(2)}(0)$ exhibits the opposite photon statistics, i.e., $g_{HH}^{(2)}(0) \simeq 1.015$ (bunching) for the output H-polarized photons under the input V-polarized photons and $g_{VV}^{(2)}(0) \simeq 0.92$ (antibunching) for the output V-polarized photons under the input H-polarized photons, respectively, at optical resonance and zero-time delay. Apart from that, the strong superbunching [55,56] with the value of $g_{HH}^{(2)}(0) \simeq 15.51$ in the output H-polarized photon statistics preferentially occurs under the input H-polarized photons. In addition, the steady-state average numbers of the products of output photonic operators are obtained, which can be used to derive the Stokes parameters and construct the Poincaré sphere. In this way, we can perform a complete polarization tomography to quantify the output polarization states. As the result of a conversion with a purely V-polarized input light, a close-to-zero-point rotation of the output polarization can be realized in the $H - V$ axis. In the meanwhile, we can also produce the diagonally and antidiagonally (D- and A-) polarized and the right-hand and left-hand (R- and L-) circularly polarized components by the conversion. A rotation by 88° can be achieved both in the latitude and longitude of the Poincaré sphere, with a polarization purity above 0.35 in the conversion from the input V-polarized photons to the output H-polarized photons. It is verified that we can realize an all-optical polarization-state conversion to enable arbitrary polarization control, by properly adjusting the frequency and polarization angle of an incident driving laser.

It is worth pointing out that the strong discrepancy between the exact numerical calculation using the full quantum master

equation and the semiclassical approximation can be found in the polarization tomography. For the polarization purity of concern, the quantum fluctuations of the cavity optomagnonic system needs to be considered. The main reason is that the degree of the quantum fluctuations is to determine the degree of the polarization purity. Supposing the quantum fluctuations (or correlations) among the TM photon, TE photon, and Kittel magnon are neglected (i.e., making the semiclassical or mean-field approximation, also the factorization approximation), the purity will be always equal to unity. Yet, beyond the semiclassical image, partial incoherence arises from the fluctuations (or correlations) experienced by the TM and TE photons and Kittel magnon. Furthermore, the polarization tomography, including Stokes parameters and polarization purity, is quite sensitive to the nature of the incoherence process.

Finally, we focus our attention on the differences between the steady-state average photon numbers in the mutual interconversions, and further shed light on this magnon-induced time-reversal asymmetry by manipulating the thermal magnons. We find that the reversal asymmetry originates from the opposite behaviors (creation and annihilation) of the intracavity magnons, and the imbalanced dissipation channels from or to the thermal reservoir in the two different transition processes. With the thermal magnon number increasing, the difference in the results of interconversion becomes smaller. It means that the time-reversal symmetry which is broken during the interconversion in the few-magnon regime is revived when the thermal magnon number rises. In addition to being of a fundamental interest, the obtained results can be employed to engineer quantum polarization states in solid-state quantum technologies and to gain new insights into the magnon-induced reversal asymmetry in the quantum cavity optomagnonics.

The rest of the paper is organized as follows: In Sec. II, we describe the cavity optomagnonic system of interest and review briefly the photon-magnon coupling mechanism, which is derived from the average electromagnetic energy in the magnetic dielectrics. At the same time, we give the optomagnonic interaction Hamiltonian of the hybrid system and the Lindblad master equation in a frame rotating, which are the bases of this work. Followed by this, we also elaborate on the feasibility for a large optomagnonic coupling coefficient. In Sec. III, we in detail discuss and analyze the polarization response based on numerical simulations. To be specific, in Sec. III A, we illustrate that the polarization-state conversion can be achieved in the driven cavity optomagnonic system. The new polarization states of photons can be produced, and subsequently the complete polarization tomography, involving the Stokes parameters, the Poincaré vector, and its modulus to assess the polarization purity and the departure from the semiclassical image is performed to quantify these available states. In Sec. III B, we are attracted to the broken reversal symmetry in the mutual interconversion between the two modes of orthogonally polarized photons. Further, we explore this magnon-induced asymmetric conversion by manipulating the magnon number. Finally, we conclude our work in Sec. IV. Appendixes A–E address supplementary technical details which are omitted in the text for readability. In particular, in Appendix E, we provide a perturbative treatment to

study the quantum features of the cavity optomagnonic model via the Schwinger-Keldysh formalism, which further supports our results.

II. PHYSICAL MODEL AND BASIC EQUATIONS

We start with introducing the physical model for the polarization-state transfer in the quantum regime based on ferromagnetic material. We consider the model of Fig. 1(a), which is similar to that adopted in Ref. [25] and consists of two optical WGMs with different polarizations and a Kittel mode. For concreteness, we use a spherical cavity made of YIG material, which is characterized by the high-Q factors for all of the excited bosons, and the wide frequency range for Fe^{3+} ironic transition in the infrared region. The bosons in the cavity are spatially overlapped, thus they can interplay with each other. The Hamiltonian of the three-mode interaction is given by (here and below, we work in units where $\hbar = 1$) [25]

$$
\begin{aligned}
\hat{H} = {} & \Omega_H \hat{a}_H^\dagger \hat{a}_H + \Omega_V \hat{a}_V^\dagger \hat{a}_V + \Omega_m \hat{m}^\dagger \hat{m} \\
& - g \hat{a}_H^\dagger \hat{a}_V (\hat{m} + \hat{m}^\dagger) - g \hat{a}_H \hat{a}_V^\dagger (\hat{m} + \hat{m}^\dagger),
\end{aligned}
\tag{1}
$$

where the symbols Ω_j are the mode frequencies of the H- and V-polarized WGM photons and the Kittel mode magnons with the subscript $j \in \{H, V, m\}$. The operators $\hat{a}_H$, $\hat{a}_V$, and $\hat{m}$ ($\hat{a}_H^\dagger$, $\hat{a}_V^\dagger$, and $\hat{m}^\dagger$) are the annihilation (creation) operators of the photons and magnons, respectively. The mode frequencies of the bosons are restrained by a frequency matching $\Omega_V - \Omega_H - \Omega_m = 0$ in YIG material, i.e., the so-called triple-resonance condition for BLS [25,26]. We have disregarded the zero-point energies of the photon and magnon modes. The interaction part of the system Hamiltonian hints that the Kittel mode magnons mediate the transfer of the polarized photons, with a photon-magnon (optomagnonic) coupling coefficient g governed by

$$
g = \int dr\, \epsilon^{\mathrm{int}}(\mathbf{M}) E_i E_j^*.
\tag{2}
$$

In the z-direction saturated magnetization configuration, the magnetization is given by $\mathbf{M} = M_x \hat{\mathbf{x}} + M_y \hat{\mathbf{y}} + M_z \hat{\mathbf{z}}$ and $M_z \simeq M_s$, $M_{x,y} \ll M_s$ with M_s being the saturation magnetization. For the given magnetization $\mathbf{M}$, the magneto-optical interaction energy is decided by the permittivity tensor $\epsilon^{\mathrm{int}}(\mathbf{M})$ with its elements $\epsilon_{ij}^{\mathrm{int}}(\mathbf{M}) = -i\epsilon_0 f \varepsilon_{ijk} M_k$, which is Faraday effect in essence. The factor ϵ_0 is the permittivity of YIG in vacuum, ε_{ijk} is the Levi-Civita symbol, f is a coefficient for quantifying the Faraday rotation [26] which can be obtained by experiments, and the subscripts i, j, k correspond to the x, y, z direction, respectively. In this paper, we consider the Voigt configuration, where an external magnetic field B is set along the z axis. In this scenario, the YIG sphere can get the full magnetization and, following [22,25], the Kittel-mode magnons can be driven by a loop coil near the YIG sphere, with a microwave frequency ω_m and a total decay rate κ_m. Optical WGMs for photons can be excited by evanescent coupling to a light source, for instance, a tapered nanofiber, an illuminated waveguide, or a prism. Additionally, in the Voigt configuration, the wave vector k of the input light goes forward on the $x - y$ plane. Hence, the magnetized YIG medium

(or the excited magnons in microcosmic) can scatter the input light (or photons) via the Faraday effect. In this process, the TM (TE) input photons propagate into the YIG cavity from a tapered fiber with an external coupling rate κ_{ex}, then are absorbed as π-spin photons and support the Fe^{3+} irons to jump from the ground states to the excited states. The excited irons immediately transition down from the excited states, to create σ^+ (σ^-) spin photons and rotate the polarization to another orthogonal plane. The polarization of σ^+ (σ^-) spin photons rotates clockwise (counterclockwise) on the $x-y$ plane (the surface of the cylinder parallel to the z axis) while they propagate along the equator of the cavity, and form a cycloid trajectory [24]. After the photons leak back to the tapered fiber, the input TM (TE) photons are converted to the TE (TM) photons. By applying this underlying mechanism, namely, the so-called spin-orbit coupling [22], the photons with H or V polarization can interchange with each other by the intermediary magnons. What is more, the output H/V-polarized photons are not coherent, as the polarization phases are changed during the travel in the cavity. The incoherence phase, brought by the magnons, plays a key role in the full quantum process. For clarification, the definition of different inputs with different transverse fields and their corresponding polarizations are shown in Fig. 1(b). The TM light corresponds to the V-polarized light, and the TE light corresponds to the H-polarized light.

In what follows, we consider the driving term of the system for analyzing the quantum polarization-state conversion. We exploit a weak-driving laser and a weak-driving microwave to satisfy a few-photon and few-magnon level. We additionally set an input polarization angle θ, which is the relative angle between the x axis (i.e., the H polarization) and the electric field (polarization) of the input light. The definition for optical polarization versus the input polarization angle θ is clearly shown by the inset of Fig. 2(a). Specifically, $\varepsilon_H = \varepsilon \cos\theta$ and $\varepsilon_V = \varepsilon \sin\theta$ are the driving amplitudes for both H and V polarizations, where ε is the total amplitude of a linearly polarized driving laser. Correspondingly, the total driving term in the polarization-state engineering with a monochromatic driving laser is then given by $\hat{H}_d = \varepsilon_H \hat{a}_H^\dagger e^{-i\omega_{in}t} + \varepsilon_V \hat{a}_V^\dagger e^{-i\omega_{in}t} + \varepsilon_m \hat{m}^\dagger e^{-i\omega_m t} + \text{H.c.}$ Thus, both of the input driving frequencies in Fig. 1(c) are equal, i.e., $\omega_{H,in} = \omega_{V,in} = \omega_{in}$. The third term and its Hermitian conjugation are included as the magnonic driving term, where ε_m is the amplitude and ω_m is the microwave frequency of the excited Kittel magnons induced by the loop coil. When we change the input polarization angle θ, the incident photons can acquire different polarization states. For example, the input photons get completely V (H) polarized when $\theta = \pi/2$ ($\theta = 0$); and when $\theta = \pi/4$, the input laser gets a balanced polarization just like it goes through a 50-50 polarizing beam splitter.

For convenience, we next switch to a frame rotating via a time-dependent unitary operator $\hat{U}(t) = \exp[i(\omega_H \hat{a}_H^\dagger \hat{a}_H + \omega_V \hat{a}_V^\dagger \hat{a}_V + \omega_m \hat{m}^\dagger \hat{m})t]$, to make the driving terms and the interaction Hamiltonian time independent. Above, ω_H indicates the frequency $\omega_{H,in}$ of the H-polarized input laser (i.e., $\omega_H = \omega_{H,in} = \omega_{in}$), ω_V indicates the frequency $\omega_{V,out}$ of the V-polarized output signal (i.e., $\omega_V = \omega_{V,out} = \omega_{in} + \omega_m$), which is just schematic illustration of the upper panel of Fig. 1(c), and vice versa (see Appendix A for further details). These two
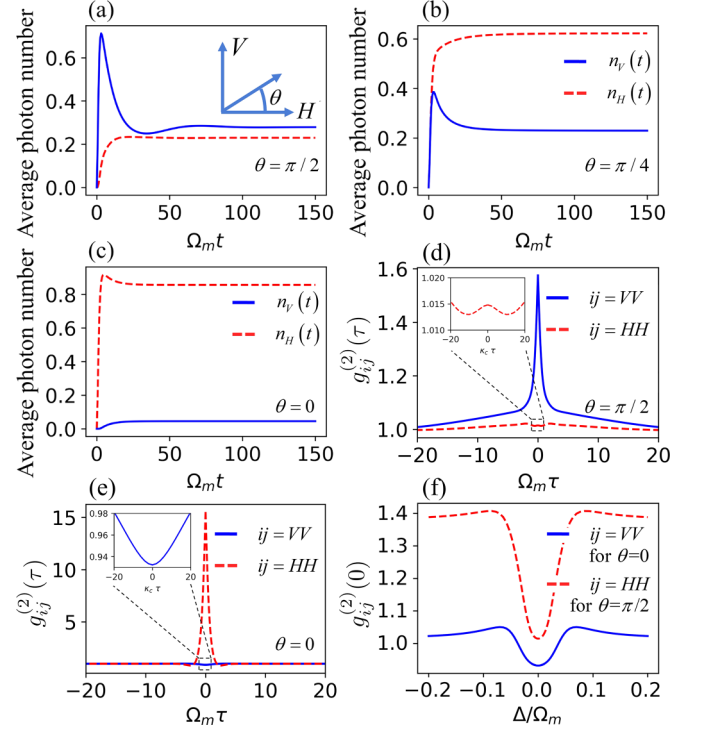

FIG. 2. (a)–(c) Time evolution of the steady-state average photon numbers $n_V(t)$ and $n_H(t)$ of the intracavity V- and H-polarized photons with different incident polarization angles: (a) $\theta = \pi/2$, (b) $\theta = \pi/4$, and (c) $\theta = 0$. The evolution time t is normalized to a dimensionless form by the magnon-mode frequency Ω_m in (a)–(c). The blue solid lines depict the average photon numbers for the V-polarized photons and the red dashed lines depict the average photon numbers for the H-polarized photons. The inset of (a) shows the definition of the input polarization angle θ. (d) The second-order correlation functions $g_{VV}^{(2)}(\tau)$ and $g_{HH}^{(2)}(\tau)$ as a function of time delay $\Omega_m \tau$ in the $\theta = \pi/2$ configuration ($ij = VV$ with blue solid line and $ij = HH$ with red dashed line). Also, the time delay τ is normalized by the magnon-mode frequency Ω_m. (e) The second-order correlation functions of V- and H-polarized photons in the $\theta = 0$ configuration. The marked line styles are set to the same as (d). The insets in (d) and (e) show the details of correlations around $\tau = 0$. The detunings are set as $\Delta_m = 0$ and $\Delta_V = \Delta_H = \Delta = 0$ for (a)–(e) above. (f) The zero-delay second-order correlations $g_{ij}^{(2)}(0)$ ($ij = HH$ for an input polarization angle $\theta = \pi/2$ and $ij = VV$ for an input polarization angle $\theta = 0$) as a function of the dimensionless detuning Δ/Ω_m. Remaining parameters are chosen as $\Omega_m = 2\pi \times 1$ GHz, $\kappa_c = 0.05\Omega_m$, $\kappa_{ex} = 0.5\kappa_c$, $\kappa_m = 2.74 \times 10^{-3}\Omega_m$, $g = 0.2\kappa_c$, $\varepsilon = 0.5\kappa_c$, $\varepsilon_m = \kappa_m$, and $n_{m,th} = 0$, respectively.

scenarios correspond to the two transition channels, as shown in Fig. 1(c). Furthermore, in conjunction with the rotating-wave approximation (RWA), the whole Hamiltonian in the frame rotating is brought to the form

$$\hat{H}_{eff} = \hat{H}_{rot} + \hat{H}_{d,rot}, \tag{3a}$$

$$\hat{H}_{rot} = -\Delta_H \hat{a}_H^\dagger \hat{a}_H - \Delta_V \hat{a}_V^\dagger \hat{a}_V - \Delta_m \hat{m}^\dagger \hat{m}$$
$$- g(\hat{a}_H^\dagger \hat{a}_V \hat{m}^\dagger + \hat{a}_H \hat{a}_V^\dagger \hat{m}), \tag{3b}$$

$$\hat{H}_{d,rot} = \varepsilon_H(\hat{a}_H^\dagger + \hat{a}_H) + \varepsilon_V(\hat{a}_V^\dagger + \hat{a}_V)$$
$$+ \varepsilon_m(\hat{m}^\dagger + \hat{m}), \tag{3c}$$

with the detuning $\Delta_j = \omega_j - \Omega_j$. In the meanwhile, we adopt the triple-resonance condition $\omega_V - \omega_H - \omega_m = 0$ inside the RWA, which is necessary to guarantee the three-boson interactions, named the magnetic BLS. The quantum system depicted by the resulting Hamiltonian in Eqs. (3a)–(3c) can effectively support the two different polarization conversion channels as follows: (i) A V-polarized photon is down-converted to an H-polarized photon by creating a magnon or (ii) an H-polarized photon is up-converted to a V-polarized photon by absorbing a magnon, both of which are shown in Fig. 1(c). More details about the model Hamiltonian are presented in Appendix A. The frequency detunings of the bosons in these two transition channels are all governed by $\Delta_V - \Delta_H - \Delta_m = 0$, according to the triple-resonance condition mentioned above.

In order to confirm our proposal, we numerically study the full quantum dynamics of this cavity optomagnonic system in the polarization-state conversion. By introducing a real-time density matrix $\hat{\rho}(t)$, the quantum Born-Markov master equation is yielded by [57–60]

$$\frac{d\hat{\rho}(t)}{dt} = i[\hat{\rho}, \hat{H}_{\text{eff}}] + \kappa_c \hat{\mathcal{D}}[\hat{a}_H]\hat{\rho} + \kappa_c \hat{\mathcal{D}}[\hat{a}_V]\hat{\rho}$$
$$+ \kappa_m(n_{m,\text{th}} + 1)\hat{\mathcal{D}}[\hat{m}]\hat{\rho} + \kappa_m n_{m,\text{th}}\hat{\mathcal{D}}[\hat{m}^\dagger]\hat{\rho} \quad (4)$$

to describe the evolution dynamics of the driven cavity optomagnonic system, where $\hat{\mathcal{D}}[\hat{O}]\hat{\rho} = \hat{O}\hat{\rho}\hat{O}^\dagger - \frac{1}{2}(\hat{O}^\dagger\hat{O}\hat{\rho} + \hat{\rho}\hat{O}^\dagger\hat{O})$ are the Lindblad dissipation superoperators, with $\hat{O} \in \{\hat{a}_H, \hat{a}_V, \hat{m}, \hat{m}^\dagger\}$. The thermal fluctuation quantum numbers of photon and magnon are governed by the Bose-Einstein distribution $n_{j,\text{th}} = \frac{1}{e^{\hbar\Omega_j/k_B T}-1}$ where the parameter k_B is the Boltzmann constant, T is the thermodynamic temperature (Kelvin), and Ω_j indicates the mode frequencies of the involved bosons, with $j \in \{H, V, m\}$ for the orthogonally polarized photons and the magnons, respectively. Here, we only consider the dissipation superoperators of the photonic annihilation operators, due to the vanishing thermal photon occupation, i.e., $n_{H(V),\text{th}} \sim 0$ at room temperature because of the high frequency of the cavity field. However, with the GHz-range magnon frequency $\Omega_m \ll \Omega_{H(V)}$, the thermal magnon number $n_{m,\text{th}}$ is much larger than $n_{H(V),\text{th}}$ at the same temperature. Thus, we need to include both dissipation channels of the magnonic operators $\hat{m}$ and $\hat{m}^\dagger$. Following Ref. [24], we set the equal decay rates of the two optical WGMs $\kappa_H = \kappa_V = \kappa_c = \kappa_{\text{in}} + \kappa_{\text{ex}}$, where κ_{in} is the intrinsic photon loss rate and κ_{ex} is the external cavity-tapered fiber coupling rate, and assume that the magnetized YIG sphere has the same internal and external decay rates $\kappa_{\text{in}} = \kappa_{\text{ex}}$, i.e., the so-called critical coupling [61,62]. Above, the intrinsic photon loss is due to the undesirable scattering and absorption from the cavity-thermal bath coupling, whereas the external photon loss is owing to the extraction of cavity photons to the desired external mode via, e.g., the cavity-tapered fiber coupling. Note that κ_{ex} can be experimentally controlled by changing the air gap between the cavity and tapered fiber [61,62].

Before proceeding, we elucidate the feasibility for a large optomagnonic coupling by optimizing the YIG cavity and utilizing the novel material. In the previous works [22,23,26], the single photon-magnon coupling coefficient is pretty weak in a sub-100-Hz range, which is in the weak-coupling regime ($g \ll \Omega_m$) as the state-of-art results. The optomagnonic coupling co-

efficient is so weak that hardly can we observe quantum effect, even in the simulations. Consequently, we can only study the cavity optomagnonic system based on the semiclassical approach, for example, by an enhanced optomagnonic coupling $G = g|\alpha|$. The steady-state amplitude of an optical control field $|\alpha|$ effectively enhances the coupling coefficient g. Furthermore, if we can achieve some optimizations to increase the overlap between the Kittel modes and the WGMs, a strong optomagnonic coupling around 100 kHz can be attained. Outside the scope of existing experiments, we can tune the driving-laser amplitude down to a weak-driving regime, and arrive at an MHz-coupling range in the meanwhile [24]. Alternatively, if a low-absorption cavity can be made of some metamaterials such as the ENZ medium, the single photon-photon-magnon coupling can be drastically enhanced to the magnon frequency range ($g \sim \Omega_m$), due to a great enhancement of the Faraday effect in essence [54]. With the consideration above, we can study full quantum dynamics in the cavity optomagnonics with a moderately strong-coupling coefficient in the following.

III. RESULTS AND ANALYSIS ABOUT POLARIZATION DYNAMICS

In this section, we begin to study the polarization dynamics of the coupled cavity optomagnonic system based on the full quantum approach. In order to describe the polarization conversion conveniently, we utilize Dirac notation to define the quantum states of H- and V-polarized photons as $|H\rangle$ and $|V\rangle$, respectively. As confirmed in Appendix A, the two transition channels $|H\rangle \rightarrow |V\rangle$ and $|V\rangle \rightarrow |H\rangle$ can both be described by the system Hamiltonian in the frame rotating, as given in Eqs. (3a)–(3c). With a tunable input laser, in the meanwhile setting different input polarizations, we can well engineer the polarization states of the output photons. To this end, taking into account the input-output formalism [58–60]

$$\hat{b}_H = b_{H,\text{in}} - i\sqrt{\kappa_{\text{ex}}}\hat{a}_H, \quad (5a)$$

$$\hat{b}_V = b_{V,\text{in}} - i\sqrt{\kappa_{\text{ex}}}\hat{a}_V, \quad (5b)$$

both of the output signals of H and V polarizations can be derived, where $b_{H,\text{in}}$ and $b_{V,\text{in}}$ are the average amplitudes of the H and V components of the applied input laser. The average values of the two orthogonal components of the input laser are defined by $b_{H,\text{in}} \equiv \varepsilon_H/\sqrt{\kappa_{\text{ex}}} = \varepsilon\cos\theta/\sqrt{\kappa_{\text{ex}}}$ and $b_{V,\text{in}} \equiv \varepsilon_V/\sqrt{\kappa_{\text{ex}}} = \varepsilon\sin\theta/\sqrt{\kappa_{\text{ex}}}$, respectively, where ε is the driving amplitude introduced before. Below, we mainly focus on three types of configurations: (i) When $\theta = \pi/2$, we have $\varepsilon_V = \varepsilon$, but $\varepsilon_H = 0$; (ii) when $\theta = 0$, we have $\varepsilon_H = \varepsilon$, but $\varepsilon_V = 0$; and (iii) when $\theta = \pi/4$, ε_H and ε_V are both equal to $\frac{\sqrt{2}}{2}\varepsilon$. In order to satisfy the few-photon regime to uncover quantum effect, the optical driving power P_{in} related to ε is set to 1 pW, which is much smaller than the power in the previous experiment [24]. On the other hand, for exciting the Kittel magnons, a bias magnetic field B is applied to form the saturated magnetization $M_s = 1.4 \times 10^5$ A/M. In the meanwhile, the other system parameters are set as $\Omega_m/2\pi = 1$ GHz, $\kappa_c = 0.05\Omega_m$, $\kappa_m = 2.74 \times 10^{-3}\Omega_m$, and $\kappa_{\text{ex}} = 0.5\kappa_c$ [12,24–26]. The driving amplitude can be derived as $\varepsilon \simeq 0.5\kappa_c$, according to the definition of average input amplitude

$\varepsilon = \sqrt{2\kappa_c P_{\text{in}}/(\hbar\omega_{\text{in}})}$, with the optical driving power $P_{\text{in}} = 1$ pW and frequency $\omega_{\text{in}}/2\pi = 200$ THz. The single photon-photon-magnon coupling strength can be correspondingly set to $g/2\pi = 10$ MHz ($g = 0.2\kappa_c$), to reveal the behaviors of the quantum cavity optomagnonic dynamics obviously. Aside from these, a weak magnonic microwave drive is brought by the loop coil with a relative amplitude chosen as $\varepsilon_m = \kappa_m$. We assume that a magnonic resonance condition $\Delta_m = 0$ holds [25,63]. According to the mode-matching condition of the frequency detunings $\Delta_V - \Delta_H - \Delta_m = 0$, the detunings of both H and V photon modes can be further simplified as the relationship $\Delta_V = \Delta_H = \Delta$. In the above configurations, we can effectively probe the traveling photons and analyze the results, to arbitrarily engineer the polarization states. At the same time, we will introduce some key parameters like the Stokes parameters and the polarization purity to quantify the polarization states of the output photons after optical conversions.

A. Controlled polarization conversion with different incident polarization angles

The thermal magnon number $n_{m,\text{th}}$ is set to zero for simplification in this subsection and the nonzero thermal magnon number will be considered in Sec. III B. First of all, we confirm whether our model can change the polarization states of the input photons or not inside the cavity. The average photon number of intracavity photons in the steady-state limit is defined by $n_l \equiv \langle \hat{a}_l^\dagger \hat{a}_l \rangle$, where the index l takes values H or V accounting for the optical polarizations. As displayed in Fig. 2 on optical resonance $\Delta = 0$, the behaviors of the conversions between two polarization states are presented. It can be seen that the full V-polarized photons transfer to the H-polarized photons when $\theta = \pi/2$ in Fig. 2(a). The definition of θ is shown in the inset in Fig. 2(a). When several V-polarized photons are pumped by the driving laser field, more than half of them are converted to the H-polarized photons. Hence, the red dashed line rises rapidly after the start of the conversion ($0 < \Omega_m t < 20$). Because some of the produced H-polarized photons have not left the cavity for a short evolution time, they can convert back to the V-polarized photons. As a result, the blue solid line (V-polarized photon number) rises up, with the red dashed line (H-polarized photon number) decreasing a little around $\Omega_m t = 50$. Then they reach the steady state after an enough evolution time $\Omega_m t > 100$. When the input polarization angle of the driving laser is fixed at $\theta = \pi/4$ in Fig. 2(b), the input photons can obtain the balanced H and V polarizations. In this case, we can see that the two sets of photons with orthogonal polarizations interchange with each other through the two conversion channels. Thus, the average photon numbers of both polarizations vary slowly until stability. When $\theta = 0$, the average photon numbers of both polarizations are plotted in Fig. 2(c), finding that the fully H-polarized photons change to the V-polarized photons on the contrary.

To gain further insight, we define a contrast factor $C_{HV} \equiv |(n_H - n_V)/(n_H + n_V)|$ here, for the comparison between the H- and V-polarized photon numbers in the steady state inside the cavity. After some calculations, the contrasts for the three initial polarizations are given by $C_{HV}(\theta = \pi/2) = 0.094$,

$C_{HV}(\theta = \pi/4) = 0.462$, and $C_{HV}(\theta = 0) = 0.900$, respectively. We find that the steady-state average photon number of H-polarized photons in Fig. 2(a) is totally different from that of V-polarized photons in Fig. 2(c), i.e., $C_{HV}(\theta = \pi/2) \neq C_{HV}(\theta = 0)$. In particular, there is an obvious gap between the blue solid line and the red dashed line in Fig. 2(b), i.e., $C_{HV}(\theta = \pi/4) \neq 0$, when the cavity optomagnonic system reaches the steady state. The clear difference and the nonzero value of the contrast factors in the interconversions above show the broken time-reversal symmetry. It suggests that the driving field with the same amplitude but different polarizations can not produce the corresponding intracavity photons which have the same average photon number. Physically, these phenomena, which reveal asymmetry in the conversions between H- and V-polarized photons, may be understood by the special bosonic transition rules in Eqs. (3a)–(3c) and the Lindblad master equation in Eq. (4). The interaction Hamiltonian [see Eq. (3b)] shows that the H mode photon creates or annihilates synchronously with a magnon. The creation channel of V-polarized photon is more heavily suppressed while the intracavity magnon is too few. This is because of the collective consumption of the quantum state conversion in the $H \rightarrow V$ process (governed by $\hat{a}_V^\dagger \hat{a}_H \hat{m}$ with the commutation relation $[\hat{a}_H, \hat{a}_V] = 0$) and the dissipation channel of $\hat{m}$ (i.e., $\kappa_m \hat{\mathcal{D}}[\hat{m}]\hat{\rho}$). More detailed discussions can be found in turn below.

On the other hand, the second-order correlation functions of the output H- and V-polarized photons as a specific example, given by [57]

$$g_{ij}^{(2)}(\tau) = \frac{\langle \hat{b}_i^\dagger(t)\hat{b}_j^\dagger(t+\tau)\hat{b}_j(t+\tau)\hat{b}_i(t) \rangle}{\langle \hat{b}_i^\dagger(t)\hat{b}_i(t) \rangle \langle \hat{b}_j^\dagger(t+\tau)\hat{b}_j(t+\tau) \rangle} \quad (6)$$

are plotted in Figs. 2(d)–2(f) to evaluate the quantum nature of optical polarization-state conversions, where t is the evolution time of the system and τ is the time delay between photon detection events. Here, the evolution time is large enough ($t \rightarrow \infty$), i.e., we consider the steady-state case for the second-order correlation function. To clarify the different photon statistics of the output polarized fields, we state the distinctions of statistics depending on $g_{ij}^{(2)}(\tau)$: When the correlations $g_{ij}^{(2)}(\tau) < 1$, these refer to photon antibunching. The values $g_{ij}^{(2)}(\tau) = 1$ represent the Poisson statistic of coherent fields; $1 < g_{ij}^{(2)}(\tau) < 2$ mean photon bunching; and $g_{ij}^{(2)}(\tau) > 2$ refer to photon superbunching [55,56]. Then, as can be seen from Fig. 2(d), under the input V-polarized photons ($\theta = \pi/2$), the second-order correlation function of the produced H-polarized photons $g_{VV}^{(2)}(\tau)$ exhibits the photon bunching effect, corresponding to the peak value $[g_{VV}^{(2)}(\tau = 0) \simeq 1.58]$. This is because of both the contributions from the input V-polarized photons and a few V-polarized photons which are converted back from H-polarized photons in the $|V\rangle \rightarrow |H\rangle$ conversion. Aside from this, we observe the slight bunching effect of the output H-polarized photons as a sign of classical photon statistics $[g_{HH}^{(2)}(\tau = 0) \simeq 1.015]$. In contrast, under the input H-polarized photons ($\theta = 0$) in Fig. 2(e), we find that the nonclassical antibunching effect appears with $g_{VV}^{(2)}(\tau = 0) \simeq 0.92$ in the $|H\rangle \rightarrow |V\rangle$ conversion, which differs a lot from the bunching effect of the produced H-polarized photons

in Fig. 2(d). With the definition of a time window ΔT when $g_{VV}^{(2)}(\tau) < 0.95$, we can see the antibunching effect with $\Delta T \simeq 20\kappa_c$ from the inset of Fig. 2(e). It reveals a long-temporal quantum property of the generated V-polarized photons in the $\theta = 0$ configuration. On the other hand, a pronounced correlation peak for the output H-polarized photons can be generated in Fig. 2(e), where $g_{HH}^{(2)}(\tau = 0) \simeq 15.51$ refers to the photon superbunching effect [55,56].

By means of the anharmonic energy levels of the cavity optomagnonic system as shown in Appendix A, there is a two-photon state at optical detuning $\Delta = 0$. This is the reason why the photon bunching effect occurs in the $\theta = \pi/2$ configuration as shown in Fig. 2(d), which is so-called two-photon collective emission. But, in the meanwhile, for the $\theta = 0$ configuration as shown in Fig. 2(e), the conventional photon antibunching can be generated due to the weak drive of H-polarized photons and the exhaustion of the intermediate magnons, namely, the low transition rate of $|H\rangle \rightarrow |V\rangle$ conversion in the weak nonlinear regime of $g = 0.2\kappa_c$. Figure 2(f) shows the second-order correlation function of the output H- and V-polarized photons in the $\theta = 0$ and $\theta = \pi/2$ configurations, respectively. It is easy to see from Fig. 2(f) that quantum statistics of photons generated by the $|H\rangle \rightarrow |V\rangle$ and $|V\rangle \rightarrow |H\rangle$ conversions are not reversible. Specifically, the minimum value (the dip) of the second-order correlation function $g_{ij}^{(2)}(\tau = 0)$ at $\Delta = 0$ exhibits the opposite photon statistical characteristics, i.e., $g_{HH}^{(2)}(0) \simeq 1.015$ (classical bunching) for the output H-polarized photons under the input V-polarized photons and $g_{VV}^{(2)}(0) \simeq 0.92$ (nonclassical antibunching) for the output V-polarized photons under the input H-polarized photons, respectively.

Next, we explore the polarization-state engineering by changing the optical detuning Δ. Here, we introduce the Stokes parameters and the Poincaré sphere to perform a tomograph of the output polarization states. The former, the Stokes parameters, defined by the intensities of three sets of orthogonally polarized fields ($H - V$, $D - A$, and $R - L$ polarized fields), includes four Stokes components in the following:

$$S_0 \equiv I_H + I_V = I_D + I_A = I_R + I_L, \tag{7a}$$

$$S_1 \equiv (I_H - I_V)/(I_H + I_V), \tag{7b}$$

$$S_2 \equiv (I_D - I_A)/(I_D + I_A), \tag{7c}$$

$$S_3 \equiv (I_R - I_L)/(I_R + I_L), \tag{7d}$$

where S_0 stands for the total intensity, or the total average photon number of an output signal at steady state. I_l is the intensity of a polarization component of the output signal given by $I_l = \langle \hat{b}_l^\dagger \hat{b}_l \rangle$, where the subscript l depicts the polarizations with $l \in \{H, V, D, A, R, L\}$. The summations of the intensities of arbitrary two orthogonal components S_0 are equal to each other, which normalizes the other three Stokes components. The normalized Stokes parameter S_1 indicates the difference of average steady-state photon numbers between H- and V-polarized states. If $S_1 = 1$ ($S_1 = -1$), the optical field is fully H (V) polarized. Likewise, the normalized Stokes parameter S_2 describes the distinction between the D and A polarizations, where the output operators in the $D - A$ bases are defined as $\hat{b}_D = (\hat{b}_H + \hat{b}_V)/\sqrt{2}$ and $\hat{b}_A = (\hat{b}_H - \hat{b}_V)/\sqrt{2}$, respectively. When the given optical field is a balanced polarized light

formed by the positive superposition (the relative polarization angle of the H and V components is $45°$) of the H- and V-polarized fields with the same amplitude, the parameters $S_1 = 0$ and $S_2 = 1$; if it is a negative superposition (the relative polarization angle of the H and V components is $135°$), then $S_1 = 0$ and $S_2 = -1$. The normalized Stokes parameter S_3 shows the dominance of R- and L-circularly polarized light, with the $R - L$ basis defined by $\hat{b}_R = (\hat{b}_H + i\hat{b}_V)/\sqrt{2}$ and $\hat{b}_L = (\hat{b}_H - i\hat{b}_V)/\sqrt{2}$. The normalized Stokes parameter S_3 evaluates the degree of circular polarization and $S_3 = 1$, 0, -1 represents the ideally R circular, linear polarization, and L circular polarizations, respectively. It also exhibits the phase shift between the H and V components.

Through setting the Stokes parameters $\{S_1, S_2, S_3\}$ as the orthogonal coordinates with a range from -1 to 1, we can construct the latter, i.e., the Poincaré sphere, and depict the quantum polarization states with it. The Poincaré vector, one-to-one mapped by the polarization state with the definition $\mathbf{v} = S_1\hat{e}_H + S_2\hat{e}_D + S_3\hat{e}_R$, shows the distribution of the polarization state and the trajectory when it changes. The approach above allows us to describe the density matrices of polarization states, which is similar to the Bloch sphere for describing the models constituted by two subsystems. From these Stokes parameters, we can derive the population of the corresponding polarization states, together with S_0. In addition, the polarization states in the quantum regime do not always be pure states after the interactions. To do this, we also introduce the polarization purity, which is given by

$$P = \sqrt{S_1^2 + S_2^2 + S_3^2}, \tag{8}$$

where the polarization purity P is normalized to 1. In the semiclassical optomechanical approach without considering quantum fluctuation of the field, the purity P is always equal to unity. This corresponds to the pure polarization states, and all of the Poincaré vectors point at the surface when the steady-state amplitude is large enough [38]. It also hints that the output polarized fields are the completely coherent superposition of the polarized fields, such as the coherent H- or V-polarized lights. However, when we study the full quantum dynamics, the incoherence and quantum fluctuation of the photons and magnons can diminish the purity of the polarization states. As a consequence, the vectors are curtailed inside the Poincaré sphere.

The tomography of the output polarized photons is clearly shown in Fig. 3, in which we still focus on the three specific input configurations mentioned before. Figures 3(a)–3(c) present the Stokes parameters $\{S_1, S_2, S_3\}$ that depict the polarization states decomposed by the corresponding orthogonal bases $\{H - V, D - A, R - L\}$. An input laser with $\theta = \pi/2$ excites coherent photons with purely V polarization, and the photons propagate in the YIG cavity. The photons preserve themselves when the driving-laser frequency is far off resonance. Hence, the Stokes parameters $S_1 \simeq -1$, $S_2 \simeq 0$, and $S_3 \simeq 0$ when the frequency detuning Δ is far away from zero, which seems like that the V-polarized light propagates through a material without dispersion. However, when the driving-laser frequency is tuned to $\Delta \simeq \pm 0.012\Omega_m$, the parameter S_1 goes larger and almost reaches zero. This hints that a balanced polarization state can be produced in the $H - V$
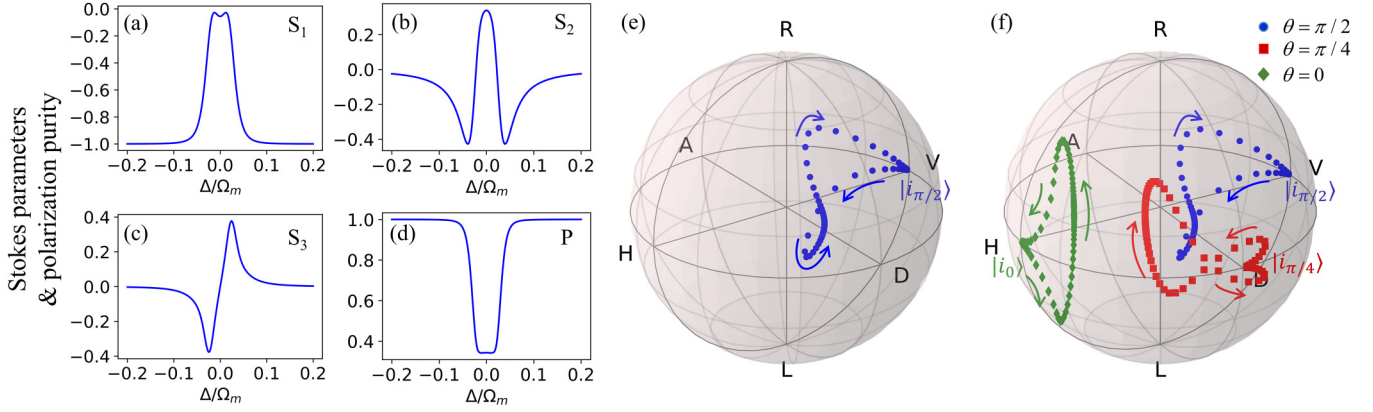
FIG. 3. Stokes parameters, polarization purity, and Poincaré spheres. (a)–(c) Stokes parameters $\{S_1, S_2, S_3\}$ as functions of the optical detuning Δ with the incident polarization angle $\theta = \pi/2$. (d) Polarization purity P plotted for the polarization-state conversion of the $|V\rangle$ to $|H\rangle$ channel with $\theta = \pi/2$. (e) Poincaré sphere plotted for the conversion of the $|V\rangle$ to $|H\rangle$ channel with $\theta = \pi/2$. The marks are displayed at the tops of the Poincaré vectors. (f) Poincaré sphere gathering the trajectories of the Poincaré vectors for three different polarization configurations with $\theta \in \{\pi/2, \pi/4, 0\}$. The blue circles are plotted for the purely V-polarized input field ($\theta = \pi/2$), the red rectangles for the $H - V$ balanced polarized input ($\theta = \pi/4$), and the green diamonds for the purely H-polarized input ($\theta = 0$). The symbols $|i_\theta\rangle$ with the corresponding colors represent the initial states in the polarization-state conversion for the above three cases, and the arrows denote the movements of the trajectories from $\Delta = -0.2\Omega_m$ to $\Delta = 0.2\Omega_m$. The other parameters are $\Omega_m = 2\pi \times 1$ GHz, $\Delta_m = 0$, $\kappa_c = 0.05\Omega_m$, $\kappa_{ex} = 0.5\kappa_c$, $\kappa_m = 2.74 \times 10^{-3}\Omega_m$, $g = 0.2\kappa_c$, $\varepsilon = 0.5\kappa_c$, $\varepsilon_m = \kappa_m$, and $n_{m,th} = 0$.

representation, just as the situation that the input light goes through a 50-50 polarization splitter. It is significant that the shallow dip at optical resonance $\Delta = 0$ shows the backward conversion from the produced H-polarized photons to the V-polarized photons. In the meanwhile, the polarization along the $D - A$ basis climbs to the maximum, corresponding to the peaks of S_2 at $\Delta = 0$ in Fig. 3(b). This is the result of the positive superposition of the balanced H- and V-polarized fields. The results obtained above confirm that the purely V polarization state of the input $|V\rangle$ photons is converted to the superpositions. Notably, when the quantum state conversion begins (the parameter S_1 starts to rise), the incoherent phase appears meanwhile (as S_3 changes). Moreover, the positions where S_1 and S_2 change rapidly in Figs. 3(a) and 3(b) correspond to the peak or dip of S_3 in Fig. 3(c). The Stokes parameter S_3 varies within a range from -0.37 to 0.37, which shows the appearance of the phase shift between the H- and V-polarized photons during the conversion. The rotating polarization, produced by the magneto-optical effect between the optical light and magnetic medium in macroscopic regime (or the interaction between the photons and magnons in microscopic regime), is the origin of the polarization-state conversion. Intuitively, the phase shift between the H and V polarization states is brought by the microwave-driving magnons. So, the elliptical polarized photons can be generated.

We notice that, in the semiclassical optomechanical approach, a strong control pump with both H and V components is necessary to realize a polarization-state conversion. Additionally, if the circularly polarized light is anticipated, a circularly polarized signal is further needed [38]. On the contrary, in our proposal, we can realize the polarization-state conversion, and acquire the elliptically polarized photons with only a linearly polarized driving laser (even with only one polarization component) in the full quantum approach. Moreover, we can reach the different elliptical polarization

states via only tuning the optical driving frequency of the linear polarized laser field, despite it is not complete enough now (with a range of about $-0.37 \sim 0.37$ for S_3). Also, the polarization purity of the configuration with a 90° incident polarization angle is plotted in Fig. 3(d). When the incident photons have not affected by the magnons at large optical detuning, the polarization purity P almost maintains a value $P \simeq 1$, corresponding to the pure polarization state. In the frequency range around optical resonance, the polarization purity drops rapidly below 0.4. It hints that we get the mixing polarization states, which is in accord with the influence of incoherent phase shift, thermal noise, and quantum fluctuation during the drastic bosonic interaction. The slightly local maximum of the polarization purity at optical resonance $\Delta = 0$ may be caused by the exchange between the input photons with $|V\rangle$ state and the produced photons with $|H\rangle$ state. Such variation tendency of the purity reveals that the incoherent components which arise from the quantum fluctuations of the output photonic fields and the magnon-induced random phase cause the decreasing polarization purity $P < 1$. The Stokes parameters with other initial incident angles, for instance, $\theta = \pi/4$ and $\theta = 0$, and more details of them are given in Appendix B.

After this, the Poincaré sphere in the configuration of $\theta = \pi/2$, i.e., with an initial state $|i_{\pi/2}\rangle = |V\rangle$, is plotted by the blue circles in Fig. 3(e) for a direct observation of the output polarization states. The Poincaré vector moves together with optical detuning Δ and forms a stereoscopically drop-like trajectory. The input photons remain at the $|V\rangle$ state in large-detuning regime, thus the vector points on the surface of the Poincaré sphere at $S_1 = -1$ (the minimum of the $H - V$ axis). Then the vector rotates and shortens inside the sphere, corresponding to the behaviors of the Stokes parameters and the polarization purity near optical resonance. As a result, in the $|V\rangle \rightarrow |H\rangle$ conversion, the trajectory of Poincaré vectors starts at the top of the V axis, excurses inside the Poincaré
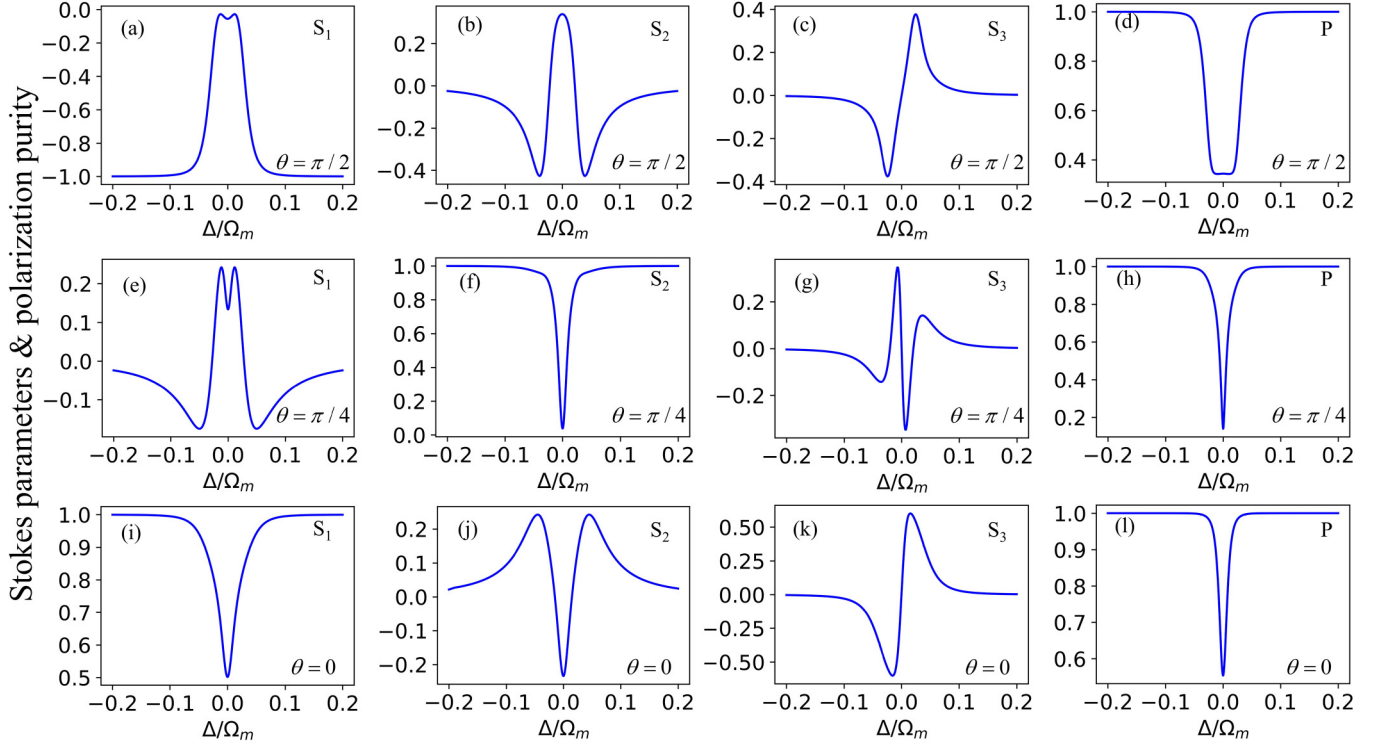
FIG. 4. Stokes parameters $\{S_1, S_2, S_3\}$ and polarization purities P for the polarization-state conversions with different initial polarizations. The pictures in the first row are plotted for the purely V-polarized input photons ($\theta = \pi/2$), the second row for the balanced polarized input photons ($\theta = \pi/4$), and the third row for the purely H input photons ($\theta = 0$). Pictures in 1 to 4 columns indicate the Stokes parameters S_1, S_2, S_3, and P, respectively. The other parameters are $\Omega_m = 2\pi \times 1$ GHz, $\Delta_m = 0$, $\kappa_c = 0.05\Omega_m$, $\kappa_{ex} = 0.5\kappa_c$, $\kappa_m = 2.74 \times 10^{-3}\Omega_m$, $g = 0.2\kappa_c$, $\varepsilon = 0.5\kappa_c$, $\varepsilon_m = \kappa_m$, and $n_{m,\text{th}} = 0$.

sphere, and returns to the beginning at the end along with the tuning of Δ. Figure 3(f) shows the trajectories of Poincaré vectors for three different initial polarization photons (with the input polarization angles $\theta \in \{\pi/2, \pi/4, 0\}$) versus the detuning Δ. As a reversal process of the $|V\rangle \rightarrow |H\rangle$ conversion, the H-polarized photons at the initial state $|i_0\rangle = |H\rangle$ transfer to the V-polarized photons when considering the input polarization angle of $\theta = 0$, plotted by the green diamonds. Obviously, there is no rotation symmetry by a 180° rotation along the R-L axis between the blue and green trajectories, which reveals a reversal asymmetry in the $|H\rangle \rightleftharpoons |V\rangle$ interconversion. The variation range of the green trajectory is smaller than the blue one in the $H-V$ basis, which corresponds to the suppression of $|H\rangle \rightarrow |V\rangle$ process by the imbalanced creation and collapse of magnons. This suppression originates from the interaction Hamiltonian and the asymmetric dissipation channels of the magnons from or to the reservoir. Although the thermal magnon number $n_{m,\text{th}} = 0$ in this subsection, there is a magnonic dissipation superoperator $\hat{\mathcal{D}}[\hat{m}]\hat{\rho}$ in the Lindblad master equation. The red rectangles, moving near the $D-A$ axis, depict the behavior of the mutual interconversion between the H- and V-polarized photons in the configuration of $\theta = \pi/4$. The quantum states during the mutual interconversion start at the initial state $|i_{\pi/4}\rangle = \frac{1}{\sqrt{2}}(|H\rangle + |V\rangle)$ and evolve into the final states which are mapped in the Poincaré sphere. In the visualization of quantum states, we can see that the red marks move to the H hemisphere [corresponding to $S_1 > 0$ in Fig. 4(e)] in the frequency range near optical resonance, which is caused by the imbalanced suppression mentioned above. It

also hints that the time-reversal symmetry of the interconversion is broken due to the appearance of the excited magnons. In the following subsection, we further show and illustrate the influence of the magnons on the polarization-state conversion and the magnon-induced reversal asymmetry.

Furthermore, in order to exhibit the unique feature of our proposal in the full quantum regime, we also simulate the polarization-state conversion via the semiclassical approximation, and show the details and results in Appendix C. The strong discrepancies between the exact numerical calculation using the full quantum master equation (4) and the semiclassical approximation in Appendix C are revealed. Physically, the vertically polarized input field (TM mode) is down-converted, whereas the horizontally polarized input field (TE mode) is up-converted, and the magnetized medium of YIG sphere (magnon mode) scatters the input photons via the Faraday effect. During this three-mode interaction beyond the semiclassical approximation, the generated field includes a contribution from the quantum fluctuations of all three modes, which are partially incoherent with respect to the input coherent fields due to the quantum correlation among the TM, TE phonons and Kittel magnon where the residual dephasing experienced by them exists. Consequently, this partial incoherence results in the strong discrepancy of Stokes parameters represented in the Poincaré sphere of Figs. 5(a) and 5(b) and also gives rise to the reduced polarization purity below unity in the blue solid line of Figs. 5(c) and 5(d). However, when the semiclassical approximation is employed, then the output field through the cavity optomagnonic system is fully coherent with
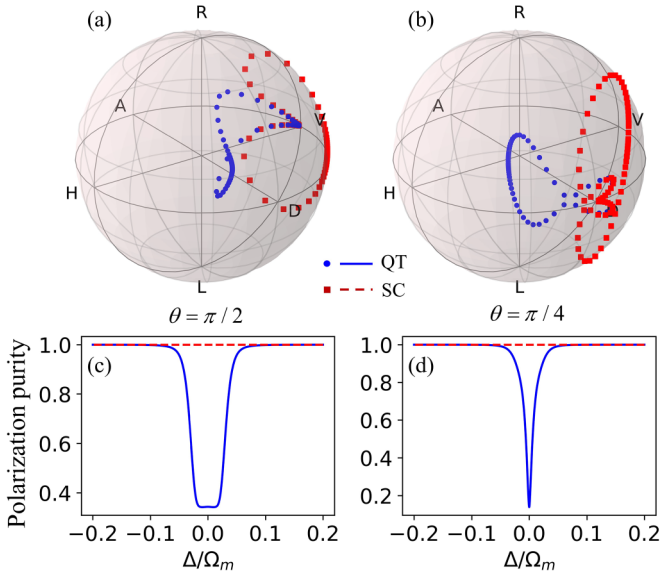
FIG. 5. Comparison between the results obtained via the full quantum approach (blue circles and solid lines) and the semiclassical approximation (red rectangles and dashed lines), which are abbreviated by "QT" and "SC" in the legend. Panels (a) and (c) are the Poincaré sphere and the polarization purity plotted for the purely V-polarized input ($\theta = \pi/2$). Panels (b) and (d) are similarly plotted for the balanced polarized driving field ($\theta = \pi/4$). The other parameters are the same as those in Fig. 4.

respect to the incident field since the quantum fluctuations around the average fields have been omitted. The output field can be entirely described by only the two expectation values $\langle \hat{b}_H \rangle$ and $\langle \hat{b}_V \rangle$. Either of them has a well-defined amplitude and phase. This brings about a completely coherent, classical superposition of horizontal and vertical polarization fields, namely, a pure polarization state in which the purity arrives at a constant value of unity as shown by the red dashed line of Figs. 5(c) and 5(d). We have performed extensive analytical calculations in Appendix C, and all results support this claim.

As a further remark, we point out that, associating with the zero-delay second-order correlation functions in Fig. 2(f), we expand more about the trajectories traveling into the inside of the Poincaré sphere, which reveals the presence of the quantum fluctuations and distinguishes the full quantum approach from the semiclassical approximation. Differing from the second-order correlation functions which are always equal to 1 via the semiclassical approach, we find that the second-order correlation functions in the full quantum regime distinctly vary in the whole frequency ranges. We can easily see that the second-order correlations $g_{ij}^{(2)}(\tau = 0)$ change a lot near optical resonance $\Delta = 0$, where the polarization-state conversions take place and the quantum fluctuations arise.

Specifically, in the semiclassical approach, where the quantum fluctuations are ignored, the second-order intensity correlation is a constant. It hints that the output polarization states are the completely coherent superposition, with a constant polarization purity $P = 1$. Thus, the trajectories of the pure output polarization states locate on the surface of the Poincaré sphere (see the details in Appendix C). On the contrary, in the full quantum regime, the second-order

correlation functions show different photon statistics for the output polarized photons under different input polarization angles in the steady-state limit. When a V-polarized input field is applied ($\theta = \pi/2$), the red dashed line in Fig. 2(f) shows the photon statistic of the produced H-polarized photons. When the trajectory on the Poincaré sphere begins to move to the inside, the phase shift between the H- and V-polarized photons becomes larger (corresponding to the larger dominance of R- and L-polarized photons), in the meanwhile the zero-delay second-order correlation function $g_{HH}^{(2)}(0)$ also becomes larger with the decrease of the detuning Δ, which shows bunching effect and means that the output H-polarized photons can be detected more possibly under a zero-time delay. On optical resonance $\Delta = 0$, the phase shift returns to zero, and the correlation goes to the minimum, but still reveals slight bunching effect with $g_{HH}^{(2)}(0) \simeq 1.015$. Similarly, in an H-polarized input configuration ($\theta = 0$), the zero-delay second-order correlation function for the produced V-polarized photons $g_{VV}^{(2)}(0)$ shows slight bunching effect under a large-detuning drive, but it refers to photon antibunching on resonance to a minimum $g_{VV}^{(2)}(0) \simeq 0.92$, where the phase shift also reduces to zero on optical resonance $\Delta = 0$. The above opposite photon statistics originate from the different behaviors of Kittel magnons in the $|H\rangle \rightleftharpoons |V\rangle$ conversions, and they also exhibit the quantum features, which deviate from the results via the semiclassical approximation.

B. Magnon-induced time-reversal asymmetry in polarization-state conversion

As we know, an external-bias magnetic field can break the time-reversal symmetry inside a solid block made of magnetic material in classical nonlinear optics [64]. For a microscopic mechanism, in the quantum cavity optomagnonics, we will show that the broken reversal symmetry can be caused and affected by the magnons. We first consider the case of a purely H-polarized input ($\theta = 0$) for finding the influence on the polarization state conversion by the thermal magnons, shown in Figs. 6(a) and 6(c). In the zero-temperature limit, there is no thermal magnon in the reservoir, i.e., $n_{m,\text{th}} = 0$. Starting at an initial state $|i_0\rangle = |H\rangle$, the trajectory of the Poincaré vectors versus the optical detuning Δ after the $|H\rangle \rightarrow |V\rangle$ conversion is plotted by the blue circles in Fig. 6(a), which is the same as the red trajectory in Fig. 3(f). When we take $n_{m,\text{th}} = 1$, the tops of the Poincaré vectors move and form a similar trajectory, but it is smaller and shifts towards the center of the Poincaré sphere, which is marked by the red rectangles. Influenced by the thermal magnons, the quantum state conversion of the $|H\rangle \rightarrow |V\rangle$ case realizes a greater conversion efficiency in the $H - V$ basis with setting the thermal magnon number $n_{m,\text{th}} = 2$. As the thermal magnon number increases, the trajectory is closer to the center of the Poincaré sphere, which means that the polarization purity decreases gradually. To clarify this phenomenon, we give a brief analysis here. During the $|H\rangle \rightarrow |V\rangle$ conversion in the $\theta = 0$ configuration, the microwave-diving magnons cannot guarantee the consumption for converting photons, as the microwave-diving amplitude of magnons ε_m is much smaller than the coupling strength g, i.e., $\varepsilon_m/g = 0.274$. The intracavity magnons can only be pumped by the microwave drive
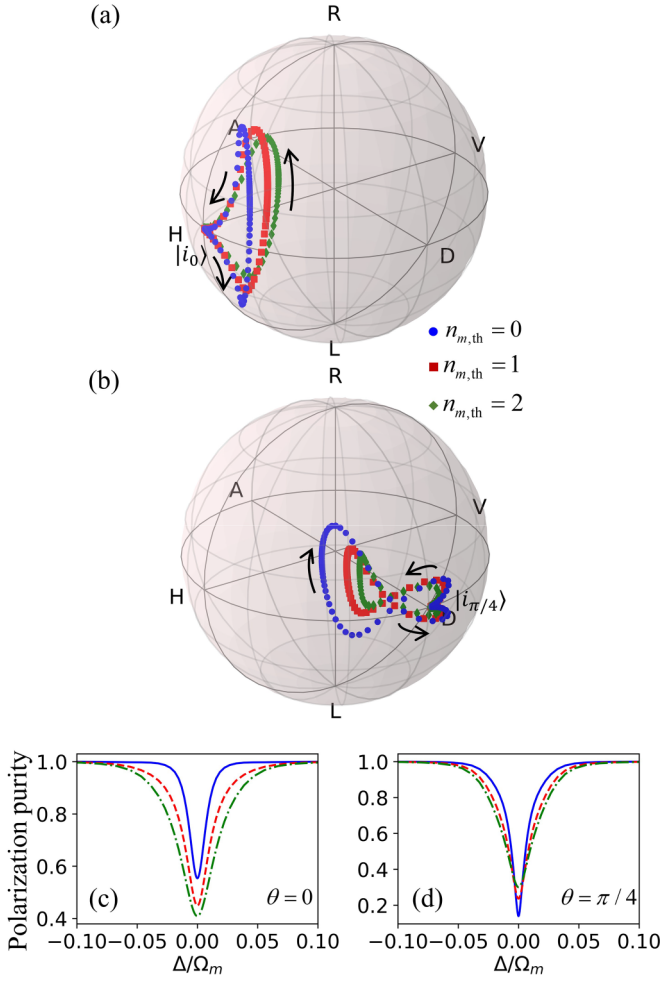
FIG. 6. Poincaré spheres and polarization purities plotted for discovering the magnon-induced incoherence and reversal asymmetry. (a) Poincaré sphere plotted for the $|H\rangle \to |V\rangle$ conversion channel with the different thermal magnon numbers $n_{m,\text{th}} \in \{0, 1, 2\}$ and the incident polarization angle $\theta = 0$. The black mark $|i_0\rangle = |H\rangle$ denotes an initial state with purely H polarization in the $\theta = 0$ case. (b) Poincaré sphere plotted for the interconversions with different $n_{m,\text{th}}$ in the same range with (a), and the input polarization angle is set to $\theta = \pi/4$. The black mark $|i_{\pi/4}\rangle = \frac{1}{\sqrt{2}}(|H\rangle + |V\rangle)$ denotes an initial state with a purely H polarization in the $\theta = \pi/4$ case. The black arrows in both of (a) and (b) stand for the movements of the trajectories versus optical detuning Δ. (c), (d) Polarization purities P with the input polarizations corresponding to (a) and (b), respectively. The blue solid lines are painted for $n_{m,\text{th}} = 0$, the red dashed lines are painted for $n_{m,\text{th}} = 1$, and the green dotted-dashed lines are painted for $n_{m,\text{th}} = 2$, corresponding to the colors of the marks in (a) and (b). The other parameters are the same as those in Fig. 3.
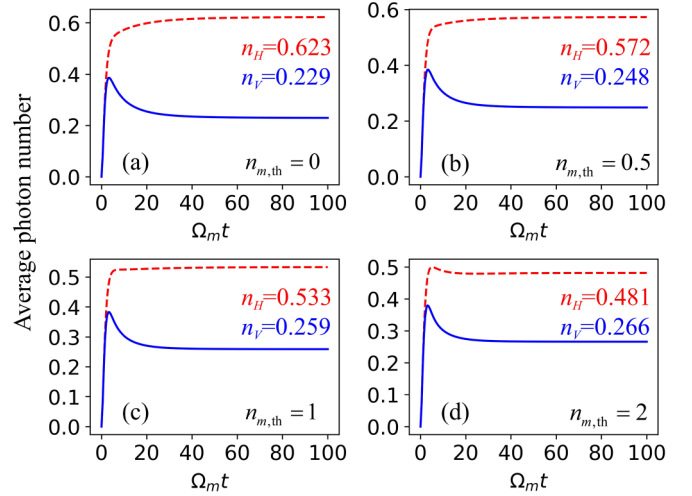

FIG. 7. Time evolution of the average photon numbers $n_H(t)$ and $n_V(t)$ of the H- and V-polarized photons in the interconversion ($\theta = \pi/4$) with the different thermal magnon numbers $n_{m,\text{th}} \in \{0, 0.5, 1, 2\}$ for (a)–(d). The red dashed and blue solid lines, respectively, depict the evolution of the photon numbers of H- and V-polarized photons. The values marked in the top-right corners of each subpicture are the steady-state average photon numbers, the colors of which correspond to the H and V polarizations in the subscripts. The other parameters are the same as those in Fig. 6.

tion in Eq. (4), and assist the microwave-driving magnons in converting the incident polarized photons. By this mechanism, the $|H\rangle \to |V\rangle$ conversion can be greatly encouraged with the increased thermal magnons. Meanwhile, the conversion range is diminished from the input H-polarized photons to the R/L-polarized photons. It hints that the thermal magnons can become the medium of the quantum state conversion between the H- and V-polarized photons, but decrease the phase shift of them. The polarization purity, which falls from $P(n_{m,\text{th}} = 0) = 0.55$ to $P(n_{m,\text{th}} = 2) = 0.4$ at optical resonance $\Delta = 0$ in Fig. 6(c), also shows the promotion for producing the mixed polarization states or the encouragement of the quantum polarization-state conversion.

For delicately studying the magnon-induced reversal asymmetry in the polarization-state conversion, we consider the interchange between the H- and V-polarized photons starting at the initial state $|i_{\pi/4}\rangle = \frac{1}{\sqrt{2}}(|H\rangle + |V\rangle)$, by applying a balanced polarized driving light with the input angle $\theta = \pi/4$. Meanwhile setting the thermal magnon number $n_{m,\text{th}} = 0$, we find a difference between the steady-state average photon numbers of the H- and V-polarized photons. With the thermal magnon number $n_{m,\text{th}}$ increasing from 0 to 2, the split between the intracavity photon numbers n_H and n_V goes smaller, meanwhile the cavity optomagnonic system can reach the steady state faster (shown in Fig. 7). We intuitively deem that this magnon-induced and magnon-influenced distinction originates from the asymmetric interaction Hamiltonian in Eq. (3b) and the imbalanced coefficients of the magnonic damping channels in the Lindblad master equation in Eq. (4). According to the interaction Hamiltonian, the H-polarized photons can only create or collapse together with both of the microwave-driving and thermal magnons during the

more slowly, relative to annihilation in the interaction with the input photons, thus the $|H\rangle \to |V\rangle$ conversion [governed by $\hat{a}_V^\dagger \hat{a}_H \hat{m}$ in Eq. (3b)] is much limited, comparing with the $|V\rangle \to |H\rangle$ conversion [governed by $\hat{a}_V \hat{a}_H^\dagger \hat{m}^\dagger$ in Eq. (3b)]. However, when the zero-temperature limit is removed, i.e., $n_{m,\text{th}} \neq 0$, the thermal magnons appear in the reservoir. The thermal magnons can enter into the cavity, governed by the collapse term $\kappa_m n_{m,\text{th}} \hat{\mathcal{D}}[\hat{m}^\dagger] \hat{\rho}$ in the Lindblad master equa-
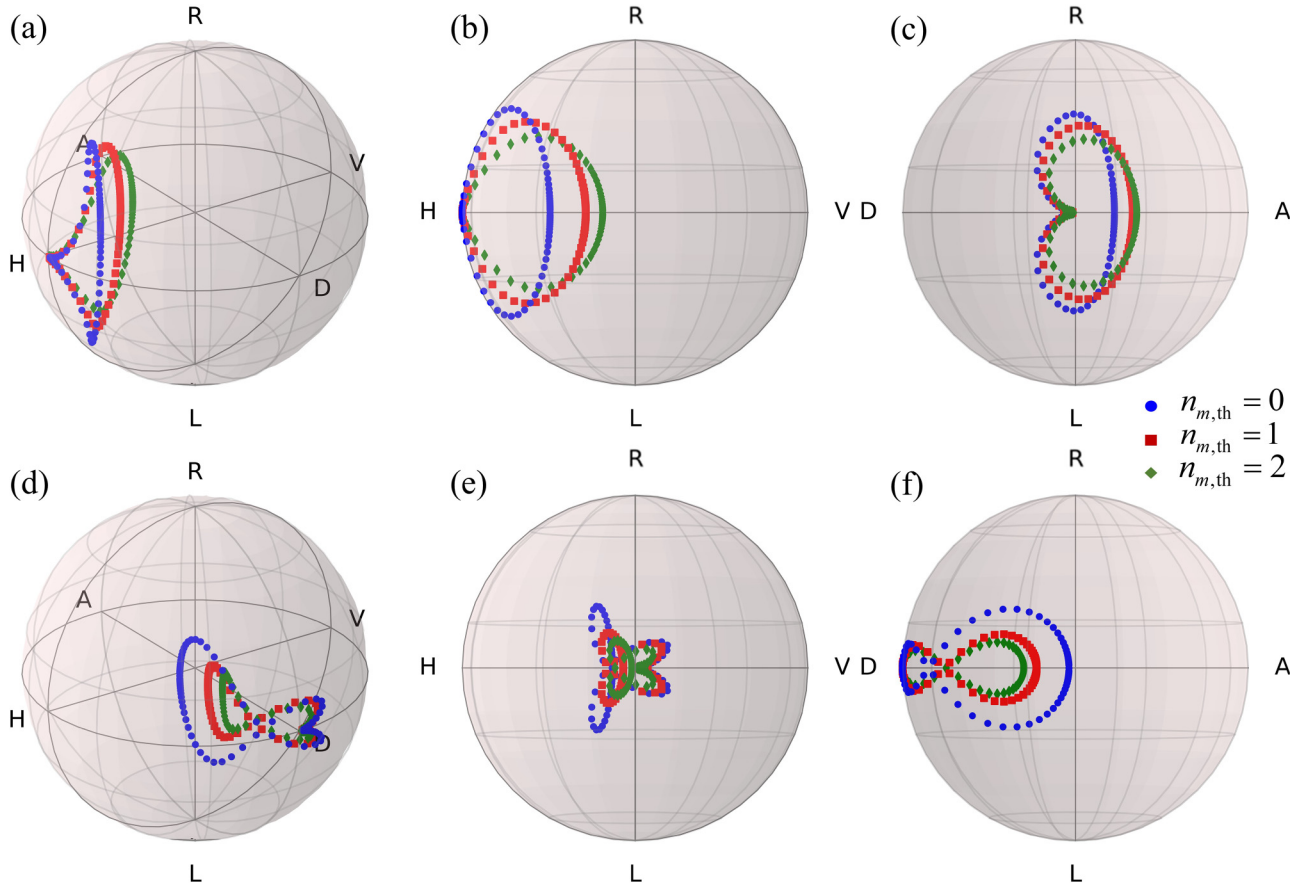
FIG. 8. Poincaré spheres for two different polarized driving fields and three thermal magnon numbers. (a)–(c) Show Poincaré spheres plotted for the purely H-polarized input ($\theta = 0$). Note that, for exhibiting every component of the Stokes parameters obviously, (b) and (c) are the two views along the $D - A$ and $H - V$ axes correspondingly. (d)–(f) A set of Poincaré spheres plotted for the balanced polarized driving field ($\theta = \pi/4$). The thermal magnon numbers are set by $n_{m,\text{th}} \in \{0, 1, 2\}$, with the corresponding colors and marks in the right side of the figure. The other parameters are the same as those in Fig. 6.

three-boson interactions. These are manifested in the products of the bosonic operators $\hat{a}_V \hat{a}_H^\dagger \hat{m}^\dagger$ and $\hat{a}_V^\dagger \hat{a}_H \hat{m}$, but without the terms $\hat{a}_V^\dagger \hat{a}_H \hat{m}^\dagger$ and $\hat{a}_V \hat{a}_H^\dagger \hat{m}$ (which is governed by another mode-matching condition $\omega_V - \omega_H + \omega_m = 0$). Additionally, the two collapse operators $\hat{\mathcal{D}}[\hat{m}]\hat{\rho}$ and $\hat{\mathcal{D}}[\hat{m}^\dagger]\hat{\rho}$ act on the density matrix of the magnonic subsystem, to control the collapse and excitation of the magnons to or from the thermal reservoir, respectively, with the imbalanced efficiency $\kappa_m(n_{m,\text{th}} + 1)$ and $\kappa_m n_{m,\text{th}}$. As a result, this cavity optomagnonic system shows the intrinsic asymmetric features, without the external asymmetric elements (such as a spin cavity [65–67] or the asymmetric control fields [43,68]). By the mechanism above, the photons can couple to not only the microwave-driving magnons, but also the thermal magnons and the magnons which are the by-products in the $|V\rangle \rightarrow |H\rangle$ conversion. In this way, the H-polarized photons can be converted more efficiently to the V-polarized photons with higher $n_{m,\text{th}}$, corresponding to the smaller difference between the steady-state average photon numbers inside the cavity.

In order to gain further insight into the magnon-induced reversal asymmetry during the interconversion process, we numerically solve the Lindblad master equation in the steady-state limit to obtain the static density matrix of the intracavity polarized photons and magnons after the $|H\rangle \rightleftharpoons |V\rangle$ intercon-

version. Additionally, by means of the input-output relations, the Stokes parameters can be calculated as the functions of the steady-state average values of the output photonic operators via Eqs. (7a)–(7d). The Poincaré sphere for the balanced polarization configuration ($\theta = \pi/4$) is shown in Fig. 6(b), and the polarization purity is displayed in Fig. 6(d). As can be seen from the figures, on the one hand, with the increase of the thermal magnon number $n_{m,\text{th}}$, the gap of the trajectory is diminished, which seems to merge along the $D - A$ axis. The output light is more similar to a balanced polarized light, with the polarization purity going smaller, i.e., the trajectory is much closer to the surface of the Poincaré sphere [as shown in Figs. 8(e) and 8(f); also see Appendix D for a detailed discussion]. It means that the reversal asymmetry of the interconversion is diminished by the increased thermal magnons. On the other hand, the thermal magnons still narrow down the conversion range in the $R - L$ basis, which is the same trend as that in Fig. 6(a). Physically, in the interconversion process, the $|H\rangle \rightarrow |V\rangle$ channel is greatly suppressed by the inadequate supply of the microwave-driving magnons and the magnonic collapse when $n_{m,\text{th}} = 0$. Consequently, the intensity of the output H-polarized photons is much larger than that of the V-polarized photons, corresponding to the blue trajectory which

shifts a lot to the H axis at optical resonance $\Delta = 0$ in Fig. 8(e). Owing to the considerably small value of $\varepsilon_m/g = 0.274$, the rate of the magnons coupling to the polarized photons is several times faster than the magnons dissipating to the reservoir, thus the optomagnonic interaction governed by $\hat{a}_V^\dagger \hat{a}_H \hat{m}$ dominates the suppression. Consequently, the intensity of the H component of the output photons is still larger than the V component with $n_{m,\mathrm{th}} = 1$. When the thermal magnon number rises to $n_{m,\mathrm{th}} = 2$, the green trajectory almost reaches the zero point of the $H - V$ axis ($S_1 = 0$) at $\Delta = 0$. What is more, the polarization purity in the off-resonance range becomes smaller with the growth of thermal magnon number, which evidences that the thermal magnons can boost the quantum state conversion. But, at optical resonance $\Delta = 0$, the polarization purity rises from $P(n_{m,\mathrm{th}} = 0) = 0.14$ to $P(n_{m,\mathrm{th}} = 2) = 0.32$. There is a tendency for the output signal to be a coherent superposition of the polarized fields, i.e., the incoherent quantum feature is diminished.

As we simulated and exhibited before, the magnon-induced reversal asymmetry of the polarization-state conversion in the cavity optomagnonic system is revealed in the full quantum regime. We illustrate that both of the microwave-driving magnons and the thermal magnons can mediate the quantum polarization-state conversion, and the thermal magnons can also induce and influence the reversal asymmetry in the interconversion. Moreover, as an intuitive extension, we predict that there will be a critical point of $n_{m,\mathrm{th}}$, where the thermal magnons can satisfy the consumption for the $|H\rangle \to |V\rangle$ conversion, and completely eliminate the reversal asymmetry in the interconversion. Beyond this critical point, the magnons can fulfill the polarization-state interconversion, so the Lindblad dissipation superoperators in the Born-Markov quantum master equation will dominate the imbalanced suppression and revive the reversal asymmetry, such as the previous experiments at the room temperature and with strong driving [24–26]. In addition, in the regime beyond the critical point, the thermal magnons diminish the incoherent quantum feature of the output polarized photons, which may bring the asymmetric process in quantum cavity optomagnonics back to the semiclassical regime, even to the classical nonlinear optics (the large amplitude difference between the two BLS sidebands, i.e., the reversal asymmetry between the up-conversion and down-conversion in Refs. [49–52]).

IV. CONCLUSIONS AND OUTLOOK

In summary, we have theoretically elaborated on an optical polarization-state engineering in the cavity optomagnonic system based on a YIG sphere in the quantum regime, and further have explored a magnon-induced time-reversal asymmetry in the polarization-state conversion. With this purpose, we present the effective Hamiltonian of the whole system to depict the two transition channels between the two polarization states $|H\rangle$ and $|V\rangle$, with a monochromatic polarization driving field and a microwave-driving field which excite both photons and magnons. For insight into the quantum regime, we set a weak-enough optical laser and a microwave-driving field to reach the few-photon and few-magnon level. By rotating the input polarization angle, we attain the input photons with three different initial polarizations. We simulate the time evo-

lution of the average photon numbers inside the cavity until steady state, to reveal the phenomenon of the polarization-state conversion. To perform the polarization tomography, we calculate the Stokes parameters to quantify the polarization states of the output photons, and paint the Poincaré spheres for mapping the polarization states, which can also represent the density matrices of the states. So, a quantum polarization-state engineering is put forward to obtain arbitrary polarization states, by appropriately tuning the frequency and the polarization angle of the input driving laser. The incoherent component arises from the quantum fluctuations around the output average field, and the magnon-induced random phase. Consequently, the output polarizations are not necessarily pure polarization states. In other words, the full quantum process is evidenced by the polarization purity $P < 1$, which is significantly different from the semiclassical approximation because the semiclassical image predicts only coherent outputs, corresponding to pure polarization states at the surface of the Poincaré sphere. In the zero-temperature limit (the thermal magnon number $n_{m,\mathrm{th}} = 0$), a polarization-state conversion approaching the zero point of the $H - V$ axis can be realized in the cases of a single-polarization incident light (H/V-polarized input is studied in the text). Meanwhile, we can even produce the elliptically polarized photons with only using the linearly polarized input photons. The phase shift can be induced to the input photons by the microwave-driving magnons in the cavity, hence, the R/L-polarized photons can be produced. For instance, the conversion of the generated polarization state $|H\rangle$, with the initial photonic polarization state $|V\rangle$, leads to a large rotation of the output polarization by $88°$ both in the latitude and longitude of the Poincaré sphere, accompanied with the slight bunching with a local maximum $g_{HH,\mathrm{max}}^{(2)}(0) \simeq 1.015$. Also, we can obtain the V-polarized photons in the $|H\rangle \to |V\rangle$ conversion, which brings a $60°$ rotation and the long-temporal nonclassical antibunching with $g_{VV,\mathrm{min}}^{(2)}(0) \simeq 0.92$.

Aside from the tomography for the polarization states, we put our eyes on the magnon-induced time-reversal asymmetry in the interconversion, due to the difference on the steady-state average photon numbers of both polarizations. We find that the magnons play an essential role in the broken time-reversal symmetry, as the magnons asymmetrically encourage and suppress the creation and collapse of the polarized photons inside the cavity. In the few-magnon regime, the microwave-driving magnons cannot satisfy the need for converting the H-polarized photons to the V-polarized photons, which means that the up-converted channel is much suppressed in the interconversion. As a result, the magnon-induced reversal asymmetry appears. With the thermal magnon number $n_{m,\mathrm{th}}$ increasing, the thermal magnons provide help to the microwave-driving magnons, thus, the magnon-induced reversal asymmetry is diminished gradually. On the one hand, the thermal magnons encourage the polarization-state conversion, evidenced by the decreasing polarization purity in the large optical detuning regime, where the microwave-driving magnons are exhausted. On the other hand, when the magnons are enough, the increasing magnons bridge a connection from the full quantum regime to the semiclassical regime, which is evidenced by the top of the Stokes vectors being closer to the surface of the Poincaré sphere in the frequency range near

optical resonance. This investigation opens up the possibility of designing a single-photon device for arbitrarily manipulating the photonic polarization states in the solid-state material, and offers a further understanding for the magnon-induced reversal asymmetry in the quantum cavity optomagnonics.

Finally, it is worth pointing out that a few natural extensions to the present investigation would be interesting directions. First of all, by analogizing to the Stokes parameters, the Poincaré vector and its modulus to assess the polarization purity and the departure from the semiclassical theory, is it possible to relate the nonclassical antibunching and classical bunching of the output polarization fields with the excursions on the surface of the Poincaré sphere? Second, what happens, for example, if the optomechanical type of coupling $g\hat{a}^{\dagger}\hat{a}(\hat{m} + \hat{m}^{\dagger})$ is taken into account? Third, can the photon-polarization change mediated by the magnon be understood intuitively by means of standard perturbation theory? For example, in Appendix E we have performed a Schwinger-Keldysh perturbation calculation for the photon-photon-magnon scattering in the cavity optomagnonic model, where we regard the optomagnonic coupling g as a perturbation to further examine its effect on the real-time optical polarization dynamics in the quantum regime. In principle, for the rest the corresponding discussions can be carried out as well. Of course, they also are arduous tasks and are left for further study in the future.

APPENDIX A: EFFECTIVE HAMILTONIAN OF TWO-CHANNEL-TRANSITION CAVITY OPTOMAGNONIC ARCHITECTURE

In the main text, we consider the two transition channels but with the same input frequency as shown in Fig. 1(c): (i) a V-polarized photon is down-converted to an H-polarized photon and (ii) an H-polarized photon to a V-polarized photon. With these in mind, the original Hamiltonian of the cavity optomagnonic system reads as

$$
\begin{aligned}
\hat{H}_{\text{ori}} = {} & \Omega_{1H}\hat{a}_{1H}^{\dagger}\hat{a}_{1H} + \Omega_{1V}\hat{a}_{1V}^{\dagger}\hat{a}_{1V} \\
& + \Omega_{2H}\hat{a}_{2H}^{\dagger}\hat{a}_{2H} + \Omega_{2V}\hat{a}_{2V}^{\dagger}\hat{a}_{2V} + \Omega_m\hat{m}^{\dagger}\hat{m} \\
& - g\hat{a}_{1H}^{\dagger}\hat{a}_{1V}(m + m^{\dagger}) - g\hat{a}_{1H}\hat{a}_{1V}^{\dagger}(m + m^{\dagger}) \\
& - g\hat{a}_{2H}^{\dagger}\hat{a}_{2V}(m + m^{\dagger}) - g\hat{a}_{2H}\hat{a}_{2V}^{\dagger}(m + m^{\dagger}), \quad \text{(A1)}
\end{aligned}
$$

which describes the two sets of H- and V-polarized WGM photons, interacting with the Kittel mode magnons. The operators and notations are defined in the main text, except that the numbers $\{1, 2\}$ mean the two transition channels. The notation 1 represents the down-conversion channel pumped by a TM input light, and the notation 2 accounts for the up-conversion

channel pumped by a TE input light. Here the driving term is introduced by $\hat{H}_d = \varepsilon_V\hat{a}_{1V}^{\dagger}e^{-i\omega_{1V}t} + \varepsilon_H\hat{a}_{2H}^{\dagger}e^{-i\omega_{2H}t} + \varepsilon_m\hat{m}^{\dagger}e^{-i\omega_m t} + \text{H.c.}$ to excite the cavity WGMs of the photons and the Kittel mode of the magnons, with the corresponding frequencies. H.c. means the Hermitian conjugate. The original Hamiltonian is so cumbersome that we try to simplify Eq. (A1). Moreover, the interaction Hamiltonian and the driving term are transformed to the time-independent forms. To this purpose, we utilize a unitary operator

$$
\hat{U}(t) = \exp\left\{i\left[\sum_{j=1,2}(\omega_{jH}\hat{a}_{jH}^{\dagger}\hat{a}_{jH} + \omega_{jV}\hat{a}_{jV}^{\dagger}\hat{a}_{jV}) + \omega_m\hat{m}^{\dagger}\hat{m}\right]t\right\}
$$

(A2)

for a frame rotating with $\hat{H} = \hat{U}\hat{H}_{\text{ori}}\hat{U}^{\dagger} - i\hat{U}(\partial\hat{U}^{\dagger}/\partial t)$, and simultaneously consider the triple-resonance condition $\omega_V - \omega_H - \omega_m = 0$, the products of operators are derived as

$$
a_{1l}^{\dagger}a_{1l} + a_{2l}a_{2l}^{\dagger} \rightarrow a_{1l}^{\dagger}a_{1l} + a_{2l}a_{2l}^{\dagger}, \quad \text{(A3a)}
$$

$$
a_{1l}^{\dagger}a_{2l} + a_{1l}a_{2l}^{\dagger} \rightarrow a_{1l}^{\dagger}a_{2l}e^{i\omega_m t} + a_{1l}a_{2l}^{\dagger}e^{-i\omega_m t}, \quad \text{(A3b)}
$$

$$
a_{jV}a_{jH}^{\dagger}m^{\dagger} + a_{j'V}a_{j'H}^{\dagger}m^{\dagger} \rightarrow a_{jV}a_{jH}^{\dagger}m^{\dagger} + a_{j'V}a_{j'H}^{\dagger}m^{\dagger}, \quad \text{(A3c)}
$$

$$
\begin{aligned}
a_{jV}a_{j'H}^{\dagger}m^{\dagger} + a_{j'V}a_{jH}^{\dagger}m^{\dagger} \rightarrow {} & a_{jV}a_{j'H}^{\dagger}m^{\dagger}e^{i\omega_m t} \\
& + a_{j'V}a_{jH}^{\dagger}m^{\dagger}e^{-i\omega_m t}, \quad \text{(A3d)}
\end{aligned}
$$

$$
\begin{aligned}
a_{jV}a_{jH}^{\dagger}m + a_{j'V}a_{j'H}^{\dagger}m \rightarrow {} & a_{jV}a_{jH}^{\dagger}m^{\dagger}e^{2i\omega_m t} \\
& + a_{j'V}a_{j'H}^{\dagger}m^{\dagger}e^{2i\omega_m t}, \quad \text{(A3e)}
\end{aligned}
$$

$$
\begin{aligned}
a_{jV}a_{j'H}^{\dagger}m + a_{j'V}a_{jH}^{\dagger}m \rightarrow {} & a_{jV}a_{j'H}^{\dagger}m^{\dagger}e^{3i\omega_m t} \\
& + a_{j'V}a_{jH}^{\dagger}m^{\dagger}e^{i\omega_m t}, \quad \text{(A3f)}
\end{aligned}
$$

where the subscript j indicates the different transition channels with $j \in \{1, 2\}$ and l indicates the H and V polarizations. Because of $\omega_m \gg g$, we can safely omit the high-frequency terms which consist of the mode-mismatching terms and the interplay terms between the different sets of photons, i.e., the so-called RWA. A relationship between the detunings of two channels is given by $\Delta_{1l} = \Delta_{2l} + \Delta_{\text{BF}}$, where Δ_{BF} originates from the magnetic birefringence for the TE and TM modes with the same orbital angular momentum. The Hamiltonian terms of the polarized photons with the geometric birefringence-induced detuning $\Delta_{\text{BF}}(\hat{a}_{2V}^{\dagger}\hat{a}_{2V} + \hat{a}_{2H}^{\dagger}\hat{a}_{2H})$ can be safely dropped, thus we can set $\Delta_{1l} = \Delta_{2l} = \Delta_l$, with $l \in \{H, V\}$. Additionally performing a transformation of the photonic modes $\hat{a}_V = \hat{a}_{1V} + \hat{a}_{2V}$ and $\hat{a}_H = \hat{a}_{1H} + \hat{a}_{2H}$, the Hamiltonian (A1) can be reduced to the form

$$
\begin{aligned}
\hat{H}_{\text{rot}} = {} & -\Delta_H\hat{a}_H^{\dagger}\hat{a}_H - \Delta_V\hat{a}_V^{\dagger}\hat{a}_V - \Delta_m\hat{m}^{\dagger}\hat{m} \\
& - g\hat{a}_H^{\dagger}\hat{a}_V\hat{m}^{\dagger} - g\hat{a}_H\hat{a}_V^{\dagger}\hat{m}. \quad \text{(A4)}
\end{aligned}
$$

Supplementally, the mentioned-above driving terms can also be transformed to a simple form $\hat{H}_{d,\text{rot}} = \varepsilon_H\hat{a}_H^{\dagger} + \varepsilon_V\hat{a}_V^{\dagger} + \varepsilon_m\hat{m}^{\dagger} + \text{H.c.}$, which is time independent. As stated above, we can exploit the effective Hamiltonian in the frame rotating to depict the cavity optomagnonic interaction of the two sets of bosons, and to simulate its dynamical evolution.

From the Hamiltonian in Eq. (A4), we analytically find some eigenstates (energy levels) of the coupled cavity optomagnonic system, and in the following we list

these anharmonic energy levels in few-photon subspace: (i) single-photon states $|\psi_1^{\pm}\rangle = \frac{1}{\sqrt{2}}(|1, 0, 0\rangle \pm |0, 1, 1\rangle)$, with an optical detuning $\Delta = \pm g$; (ii) a two-photon singlet $|\psi_2^0\rangle = \frac{1}{3}(\sqrt{6}|2, 0, 0\rangle - \sqrt{3}|0, 2, 2\rangle)$, with an optical resonance condition $\Delta = 0$; and (iii) the two-photon doublets $|\psi_2^{\pm}\rangle = \frac{1}{\sqrt{6}}(|2, 0, 0\rangle \pm \sqrt{3}|1, 1, 1\rangle + \sqrt{2}|0, 2, 2\rangle)$, with a detuning $\Delta = \pm\frac{\sqrt{6}}{2}g$, correspondingly. The notation $|n_V, n_H, n_m\rangle$ represents the Fock state with n_V V-polarized photons, n_H H-polarized photons, and n_m Kittel magnons.

APPENDIX B: OPTICAL POLARIZATION-STATE TOMOGRAPHY

During the polarization-state conversion, we need to define some key parameters for quantifying the output polarization states. Thus, the Stokes parameters and the polarization purity are introduced. Deriving from the input-output formalism for H- and V-polarized output fields, and the definition of the other output operators $\hat{b}_l$ in the main text, the complete input-output relations of all the orthogonal polarization bases are given by

$$\hat{b}_H = b_{H,\text{in}} - i\sqrt{\kappa_{\text{ex}}}\hat{a}_H, \tag{B1a}$$

$$\hat{b}_V = b_{V,\text{in}} - i\sqrt{\kappa_{\text{ex}}}\hat{a}_V, \tag{B1b}$$

$$\hat{b}_D = b_{D,\text{in}} - i\sqrt{\kappa_{\text{ex}}}\hat{a}_D, \tag{B1c}$$

$$\hat{b}_A = b_{A,\text{in}} - i\sqrt{\kappa_{\text{ex}}}\hat{a}_A, \tag{B1d}$$

$$\hat{b}_R = b_{R,\text{in}} - i\sqrt{\kappa_{\text{ex}}}\hat{a}_R, \tag{B1e}$$

$$\hat{b}_L = b_{L,\text{in}} - i\sqrt{\kappa_{\text{ex}}}\hat{a}_L, \tag{B1f}$$

with additional definitions $b_{D/A,\text{in}} = (b_{H,\text{in}} \pm b_{V,\text{in}})/\sqrt{2}$, $b_{R/L,\text{in}} = (b_{H,\text{in}} \pm ib_{V,\text{in}})/\sqrt{2}$, $\hat{a}_{D/A} = (\hat{a}_H \pm \hat{a}_V)/\sqrt{2}$, and $\hat{a}_{R/L} = (\hat{a}_H \pm i\hat{a}_V)/\sqrt{2}$ (the subscripts D and R correspond to the symbol "+" while A and L correspond to "−"). In above equations, $\hat{b}_l$ ($\hat{b}_l^{\dagger}$) are the annihilation (creation) operators of the corresponding output polarized photons, $\hat{a}_l$ ($\hat{a}_l^{\dagger}$) are the annihilation (creation) operators of the corresponding input polarized photons, and $b_{l,\text{in}}$ are the average amplitude of the input fields in the corresponding polarization bases. Owing to the linearly polarized input light we set, the average amplitude of the R and L components are always equal to

zero. Accordingly, the terms $b_{R,\text{in}}$ and $b_{L,\text{in}}$ are absent in Eqs. (B1e)–(B1f). The components of the Stokes parameters have been defined in the main text, as the form in the following:

$$S_0 \equiv I_H + I_V = I_D + I_V = I_R + I_L, \tag{B2a}$$

$$S_1 \equiv (I_H - I_V)/(I_H + I_V), \tag{B2b}$$

$$S_2 \equiv (I_D - I_A)/(I_D + I_A), \tag{B2c}$$

$$S_3 \equiv (I_R - I_L)/(I_R + I_L), \tag{B2d}$$

where I_l is the intensity of a polarization component of the output signal given by $I_l = \langle \hat{b}_l^{\dagger}\hat{b}_l \rangle$, where the subscript l depicts the polarizations with $l \in \{H, V, D, A, R, L\}$.

Furthermore, by introducing the definition of the $D - A$ and $R - L$ orthogonal bases

$$\hat{b}_D = (\hat{b}_H + \hat{b}_V)/\sqrt{2}, \tag{B3a}$$

$$\hat{b}_A = (\hat{b}_H - \hat{b}_V)/\sqrt{2}, \tag{B3b}$$

$$\hat{b}_R = (\hat{b}_H + i\hat{b}_V)/\sqrt{2}, \tag{B3c}$$

$$\hat{b}_L = (\hat{b}_H - i\hat{b}_V)/\sqrt{2}, \tag{B3d}$$

we can simplify the Stokes parameters to the functions of only the output photonic operators in the $H - V$ representation, which are yielded by

$$S_0 = I_H + I_V, \tag{B4a}$$

$$S_1 = \frac{\langle \hat{b}_H^{\dagger}\hat{b}_H \rangle - \langle \hat{b}_V^{\dagger}\hat{b}_V \rangle}{I_H + I_V}, \tag{B4b}$$

$$S_2 = \frac{\langle \hat{b}_H^{\dagger}\hat{b}_V \rangle + \langle \hat{b}_H\hat{b}_V^{\dagger} \rangle}{I_H + I_V}, \tag{B4c}$$

$$S_3 = i\frac{\langle \hat{b}_H^{\dagger}\hat{b}_V \rangle - \langle \hat{b}_H\hat{b}_V^{\dagger} \rangle}{I_H + I_V}. \tag{B4d}$$

The Dirac brackets $\langle \cdot \rangle$ indicate the average values of the operators inside them in the steady-state limit, which can be calculated with the steady-state density matrix ($t \to \infty$) by solving the Lindblad master equation (4). Then, substituting the output operators $\hat{b}_l$ ($\hat{b}_l^{\dagger}$) by Eqs. (B1a)–(B1f) into Eqs. (B4a)–(B4d), the Stokes parameters are derived as

$$S_0 = I_H + I_V = \kappa_{\text{ex}}\langle 1 + i\cos\theta(\hat{a}_H^{\dagger} - \hat{a}_H) + i\sin\theta(\hat{a}_V^{\dagger} - \hat{a}_V) + (\hat{a}_H^{\dagger}\hat{a}_H + \hat{a}_V^{\dagger}\hat{a}_V)\rangle, \tag{B5a}$$

$$S_1 = \frac{\kappa_{\text{ex}}\langle (\cos^2\theta - \sin^2\theta) + i\cos\theta(\hat{a}_H^{\dagger} - \hat{a}_H) - i\sin\theta(\hat{a}_V^{\dagger} - \hat{a}_V) + (\hat{a}_H^{\dagger}\hat{a}_H - \hat{a}_V^{\dagger}\hat{a}_V)\rangle}{I_H + I_V}, \tag{B5b}$$

$$S_2 = \frac{\kappa_{\text{ex}}\langle 2\cos\theta\sin\theta + i\cos\theta(\hat{a}_V^{\dagger} - \hat{a}_V) + i\sin\theta(\hat{a}_H^{\dagger} - \hat{a}_H) + (\hat{a}_H^{\dagger}\hat{a}_V + \hat{a}_H\hat{a}_V^{\dagger})\rangle}{I_H + I_V}, \tag{B5c}$$

$$S_3 = \frac{\kappa_{\text{ex}}\langle \cos\theta(\hat{a}_V^{\dagger} + \hat{a}_V) - \sin\theta(\hat{a}_H^{\dagger} + \hat{a}_H) + i(\hat{a}_H^{\dagger}\hat{a}_V - \hat{a}_H\hat{a}_V^{\dagger})\rangle}{I_H + I_V}. \tag{B5d}$$

Based upon Eqs. (B5a)–(B5d), we can evaluate the Stokes parameters and perform the complete tomography for the polarization-state engineering in the Poincaré sphere. We nu-

merically simulate the polarization-state conversion in three types of configurations with the following different input polarization angles: (i) $\theta = \pi/2$, (ii) $\theta = \pi/4$, and (iii) $\theta = 0$,

respectively. The results are displayed in Fig. 4, where the Stokes parameters and the purity of the output polarization states are plotted as a function of the optical detuning Δ for three different polarization angles θ.

APPENDIX C: COMPARISON BETWEEN SEMICLASSICAL APPROXIMATION AND FULL QUANTUM APPROACH

As we know, the semiclassical approximation is widely used in the analyses of quantum state conversion by linearizing an operator and making the Hamiltonian to a "beam-splitter" form [39–43]. In the weak-driving and weak-coupling regimes, the semiclassical approximation is an appropriate method to solve the problem in quantum state conversion, in which a linearization $\hat{\mathcal{O}} = \langle \hat{\mathcal{O}} \rangle + \delta \hat{\mathcal{O}}$ with a coherent term $\langle \hat{\mathcal{O}} \rangle$ and a quantum incoherent term $\delta \hat{\mathcal{O}}$ is generally suitable for an arbitrary operator $\hat{\mathcal{O}}$. In this way, for example, the expectation value $\langle \hat{b}_l \rangle$ describes the optical output field of $\hat{b}_l$ with $l \in \{H, V, D, A, R, L\}$, and the output intensity can be given by $I_l = \langle \hat{b}_l^\dagger \rangle \langle \hat{b}_l \rangle$, with neglecting the fluctuation terms. In the semiclassical approximation, the quantum fluctuations around the expectation values can be omitted, as the output fields are expected for coherent fields in the polarization-state conversion. However, in our work, the quantum fluctuations lead a lot of incoherent components to the output fields, thus the results of the exact quantum master equation calculations are obviously different from what are obtained by the semiclassical approximation. In the main text, we have displayed the detailed results in the quantum regime. Then, in this Appendix, we show the analysis and give the simulation results with semiclassical approximation for a comparison.

By including the dissipations and input fields of the photon and magnon modes, in the meanwhile turning the cavity optomagnonic system to the interaction picture with the unitary operator $\hat{U}(t)$ [Eq. (A2)] and combining the effective Hamiltonian [Eqs. (3a) and (3b)], the quantum Langevin equations (QLEs) of the whole driven system can be given by

$$\dot{a}_H = \left(i\Delta_H - \frac{\kappa_H}{2} \right) \hat{a}_H + ig\hat{a}_V \hat{m}^\dagger - i\varepsilon_H - i\sqrt{\kappa_{\rm in}} \hat{f}_{H,\rm in},$$
$$\text{(C1a)}$$

$$\dot{a}_V = \left(i\Delta_V - \frac{\kappa_V}{2} \right) \hat{a}_V + ig\hat{a}_H \hat{m} - i\varepsilon_V - i\sqrt{\kappa_{\rm in}} \hat{f}_{V,\rm in},$$
$$\text{(C1b)}$$

$$\dot{m} = \left(i\Delta_m - \frac{\kappa_m}{2} \right) \hat{m} + ig\hat{a}_H^\dagger \hat{a}_V - i\varepsilon_m - i\sqrt{\frac{\kappa_m}{2}} \hat{f}_{m,\rm in}.$$
$$\text{(C1c)}$$

The operators $\hat{f}_{H,\rm in}$, $\hat{f}_{V,\rm in}$, and $\hat{f}_{m,\rm in}$ are the input noises introduced for the H- and V-polarized photons and the Kittel magnons, and the definitions of other parameters are the same as those in the main text. The involved input-noise operators have zero average values, i.e., $\langle \hat{f}_{l,\rm in} \rangle = 0$. Alternatively, the nonzero correlation functions of input operators are exhibited as follows: $\langle \hat{f}_{H,\rm in}(t) \hat{f}_{H,\rm in}^\dagger(t') \rangle = \delta(t - t')$, $\langle \hat{f}_{V,\rm in}(t) \hat{f}_{V,\rm in}^\dagger(t') \rangle = \delta(t - t')$, $\langle \hat{f}_{m,\rm in}(t) \hat{f}_{m,\rm in}^\dagger(t') \rangle = (n_{m,\rm th} +$

$1)\delta(t - t')$, and $\langle \hat{f}_{H,\rm in}^\dagger(t) \hat{f}_{H,\rm in}(t') \rangle = n_{m,\rm th} \delta(t - t')$ [69]. The thermal quantum numbers are assumed as $n_{H(V),\rm th} \sim 0$ at room temperature, and $n_{m,\rm th} \gg n_{H(V),\rm th}$, which are the same definition in Sec. II of the main text. Under the continuous-wave drives, the system can evolve to a steady state. We linearize the operators by rewriting a bosonic operator as a classical average value plus a quantum fluctuation operator $\hat{\mathcal{O}} = \langle \hat{\mathcal{O}} \rangle + \delta \hat{\mathcal{O}}$, with $\hat{\mathcal{O}} \in \{\hat{a}_H, \hat{a}_V, \hat{m}\}$. In the meanwhile, the second-order terms of the fluctuation operators are generally neglected, and we apply the semiclassical approximation with $\langle \hat{a}_V \hat{m}^\dagger \rangle = \langle \hat{a}_V \rangle \langle \hat{m}^\dagger \rangle$, $\langle \hat{a}_H \hat{m} \rangle = \langle \hat{a}_H \rangle \langle \hat{m} \rangle$, and $\langle \hat{a}_H^\dagger \hat{a}_V \rangle = \langle \hat{a}_H^\dagger \rangle \langle \hat{a}_V \rangle$. In this way, according to the QLEs (C1a)–(C1c), we can directly derive two sets of equations for the classical average values and quantum fluctuation operators. Still applying the resonance condition of magnons $\Delta_m = 0$, i.e., $\Delta_V = \Delta_H = \Delta$, and meanwhile considering the zero average values of the input noise terms, we can simplify the average-value equations to the nonlinear equations in the following:

$$\langle \hat{a}_H \rangle = \frac{-D_H + G_V \langle \hat{m}^\dagger \rangle}{\left[-\tilde{\Delta}^2 - i\frac{\Delta(\kappa_H + \kappa_V)}{2} \right] + g^2 \langle \hat{m}^\dagger \rangle \langle \hat{m} \rangle}, \quad \text{(C2a)}$$

$$\langle \hat{a}_V \rangle = \frac{-D_H + G_V \langle \hat{m} \rangle}{\left[-\tilde{\Delta}^2 - i\frac{\Delta(\kappa_H + \kappa_V)}{2} \right] + g^2 \langle \hat{m}^\dagger \rangle \langle \hat{m} \rangle}, \quad \text{(C2b)}$$

$$\langle \hat{m} \rangle = \frac{2i(D_H + G_V \langle \hat{m}^\dagger \rangle)(D_V + G_H \langle \hat{m} \rangle)}{\kappa_m(-\tilde{\Delta}^2 + g^2 \langle \hat{m}^\dagger \rangle \langle \hat{m} \rangle)^2 + \frac{\kappa_m \Delta^2(\kappa_H + \kappa_V)^2}{4}}, \quad \text{(C2c)}$$

in which the associated coefficients are defined as $D_H = \varepsilon_H \Delta + i\frac{\varepsilon_H \kappa_V}{2}$, $D_V = \varepsilon_V \Delta + i\frac{\varepsilon_V \kappa_H}{2}$, $G_V = g\varepsilon_V$, $G_H = g\varepsilon_H$, $\tilde{\Delta}^2 = \Delta^2 - \frac{\kappa_H \kappa_V}{4}$, and $\langle \hat{m}^\dagger \rangle = \langle \hat{m} \rangle^\dagger$. Because of the high-order nonlinear equation for the steady-state average values of magnons in Eq. (C2c), we can hardly yield the analytical solutions of the QLEs. Hence, we try to calculate the steady-state average values based on QLEs [see Eqs. (C2a)–(C2c)] and, at the same time, numerically solve the master equation in Eq. (4), and show the distinction of the Poincaré sphere between the full quantum approach and the semiclassical image.

As shown in Fig. 5, the polarization-state conversions behave completely different in what are obtained between the full quantum regime and the semiclassical regime. With the semiclassical approximation $\langle \hat{\mathcal{O}}_i^\dagger \hat{\mathcal{O}}_j \rangle = \langle \hat{\mathcal{O}}_i^\dagger \rangle \langle \hat{\mathcal{O}}_j \rangle$, the quantum fluctuations around the steady-state average values in the QLEs are not considered, which contain abundant incoherent components of the output fields $\hat{b}_l$ and bring full quantum features to our work. The blue circles and solid lines in Fig. 5 are the results in the full quantum regime. On the contrary, the trajectories plotted with red rectangles all locate on the surface of Poincaré sphere, which hint the purely coherent output fields after the polarization-state conversions. It can also be confirmed that the polarization purity in Figs. 5(c) and 5(d) equal to unity throughout all of detuning Δ. For a short summary, the comparison in this section exhibits the great difference between the full quantum and semiclassical approaches in our work, and the Poincaré sphere clearly visualizes the difference. On the one hand, in the semiclassical approach, the fields are generally regarded as averages, thus the output fields are always the fully coherent superpositions, i.e., the so-called pure polarization states ($P = 1$). On the other hand, the essential feature, quantum fluctuations, bring

the incoherent components to the output photons after the quantum polarization-state conversion, hence the trajectories move into the inside of Poincaré sphere, and the polarization purities decrease ($P < 1$).

Besides, it should be stressed that the zero-delay second-order correlation functions of the output polarized photons always equal to 1 in the steady-state limit via the semiclassical approach, such as

$$
\begin{aligned}
g^{(2)}_{HH}(0) &= \langle \hat{b}^{\dagger}_H \hat{b}^{\dagger}_H \hat{b}_H \hat{b}_H \rangle / \langle \hat{b}^{\dagger}_H \hat{b}_H \rangle^2 \\
&= \frac{|c_H|^4 (b^*_{H,\mathrm{in}} + i\sqrt{\kappa_{\mathrm{ex}}}\alpha^*_H)(b^*_{H,\mathrm{in}} + i\sqrt{\kappa_{\mathrm{ex}}}\alpha^*_H)(b_{H,\mathrm{in}} - i\sqrt{\kappa_{\mathrm{ex}}}\alpha_H)(b_{H,\mathrm{in}} - i\sqrt{\kappa_{\mathrm{ex}}}\alpha_H)}{[|c_H|^2 (b^*_{H,\mathrm{in}} + i\sqrt{\kappa_{\mathrm{ex}}}\alpha^*_H)(b_{H,\mathrm{in}} - i\sqrt{\kappa_{\mathrm{ex}}}\alpha_H)]^2} = 1
\end{aligned}
\tag{C3a}
$$

for the output H-polarized photons, where the final polarization state is a complete superposition of the coherent state, i.e., $|\psi_{\mathrm{ss}}\rangle = c_H|\alpha_H\rangle + c_V|\alpha_V\rangle$ according to the trajectories on the surface of the Poincaré sphere under the semiclassical approximation. The output operator $\hat{b}_H$ has been introduced before, the state $|\psi_{\mathrm{ss}}\rangle$ is a final state which has evolved to the steady-state limit, the factors c_H and c_V are the probability amplitudes of corresponding coherent states $|\alpha_H\rangle$ and $|\alpha_V\rangle$. Obviously, the coherent state $|\alpha_H\rangle$ is an eigenstate of the output operator $\hat{b}_H$ (annihilation operator $\hat{a}_H$) with the eigenvalue α_H. This leads the second-order correlation function to a constant in Eq. (C3a), i.e., $g^{(2)}_{HH}(0) = 1$ (we have confirmed it in numerical simulation but have not shown it here), which hints that the output polarized fields are actually coherent fields. It also differs a lot from the results in the full quantum level as mentioned in the main text [Fig. 2(f)], and further offers another view of the comparison between the semiclassical approximation and full quantum approach.

APPENDIX D: MAGNON-INDUCED REVERSAL ASYMMETRY IN POLARIZATION-STATE CONVERSION

When we apply a balanced polarized input field and assume the zero-temperature limit $n_{m,\mathrm{th}} = 0$, we can find a difference between the steady-state average photon numbers of the H- and V-polarized photons. We intuitively deem that this asymmetry originates from the asymmetric interaction Hamiltonian in Eq. (A3) and the imbalanced damping channels in the Lindblad master equation (4). In the optomagnonic interplay between the H- and V-polarized photons and the magnons, the H-polarized photons can only create or annihilate together with the excited magnons. They are the forms of the products of bosonic operators $\hat{a}_V \hat{a}^{\dagger}_H \hat{m}^{\dagger}$ and $\hat{a}^{\dagger}_V \hat{a}_H \hat{m}$ governed by the triple-resonance condition $\omega_V - \omega_H - \omega_m = 0$, but without the terms $\hat{a}_V \hat{a}^{\dagger}_H \hat{m}$ and $\hat{a}^{\dagger}_V \hat{a}_H \hat{m}^{\dagger}$ which are governed by another mode-matching condition $\omega_V - \omega_H + \omega_m = 0$. In addition, the two collapse operators $\hat{\mathcal{D}}[\hat{m}]\hat{\rho}$ and $\hat{\mathcal{D}}[\hat{m}^{\dagger}]\hat{\rho}$ apply to the density matrix of the magnonic subsystem, for controlling the collapse and thermal excitation of magnons to and from the thermal reservoir, with the imbalanced efficiencies $\kappa_m(n_{m,\mathrm{th}} + 1)$ and $\kappa_m n_{m,\mathrm{th}}$. These two mode-matching conditions are dependent on the direction of the external bias magnetic field [26], with $+z$ and $-z$, respectively. Consequently, this cavity optomagnonic system shows an intrinsic asymmetry based on the magneto-optical effect, i.e., the Faraday effect here. We delicately study the intracavity photon numbers in the $\theta = \pi/4$ configuration, and show the results in Fig. 7. The contrast factors for

the four cases with different thermal magnon number $n_{m,\mathrm{th}}$ are shown as $C_{HV}(n_{m,\mathrm{th}} = 0) = 0.462$, $C_{HV}(n_{m,\mathrm{th}} = 0.5) = 0.395$, $C_{HV}(n_{m,\mathrm{th}} = 1) = 0.346$, and $C_{HV}(n_{m,\mathrm{th}} = 2) = 0.288$. These factors reveal that the interconversion is much influenced by the thermal magnons. When the thermal magnon number $n_{m,\mathrm{th}}$ increases, the contrast between the H- and V-polarized photon numbers decreases, which means that the magnon-enhanced asymmetry is diminished.

Alternatively, the Poincaré spheres plotted for the different thermal magnon numbers and the different input polarizations are shown in Fig. 8. Figures 8(a)–8(c) describe the changes of the Poincaré vectors with a purely H-polarized input, influenced by the increasing thermal magnons. We can easily see that the $|H\rangle \rightarrow |V\rangle$ conversion is encouraged by the increasing thermal magnons. But the channels are suppressed for the conversion to the $|R/L\rangle$ states, which implies that the thermal magnons can bring less phase information to the incident H/V-polarized photons. Correspondingly, the green trajectory is closer to the center than the blue and red marks, which means that the more thermal magnons can help the microwave-driving magnons to perform the full quantum state transfer, and make the polarization states of the output photons be more similar to the mixed polarization states (the polarization purity P is much smaller than 1). Figures 8(d)–8(f) are plotted for the balanced polarization configuration. In the views along the $D - A$ or $H - V$ axes, we can obviously see that the asymmetry is greatly diminished by the increasing thermal magnon number $n_{m,\mathrm{th}}$. If the conversions of $|H\rangle \rightarrow |V\rangle$ and $|V\rangle \rightarrow |H\rangle$ totally obey the reversal symmetry, we can only obtain a point in Fig. 8(e) and a line in Fig. 8(f). Analogously, the purity of the polarization states approaches a constant value close to 1 in the near-resonance range when $n_{m,\mathrm{th}}$ goes larger, corresponding to the blue$\rightarrow$ red $\rightarrow$green order.

APPENDIX E: PHOTON-PHOTON-MAGNON SCATTERING PROBLEM FROM A SCHWINGER-KELDYSH CALCULATION

For the further study on the BLS scattering in the cavity optomagnonic system, which is the essence of the optical polarization-state interconversion in our work, we follow the Schwinger-Keldysh formalism [70] to obtain the scattering properties of the involved bosons. As an alternative way for the scattering problem, the Schwinger-Keldysh formalism is a pure quantum mechanical process, thus, it can help to confirm our analysis of the produced (scattered) polarized photons in the main text.

In the Schwinger-Keldysh formalism, we can take apart the total Hamiltonian of a many-body system to study a real-time perturbation theory of this quantum system [70]. Generally, we set a trivial part as the unperturbed Hamiltonian $\hat{H}_0$ (e.g., the free Hamiltonian of bosons), and the remaining part is the nontrivial perturbed terms $\hat{H}_1$ (e.g., the interaction Hamiltonian). In the perturbative treatment, as a well-known paradigm in standard textbooks of quantum mechanics, we can consider a real-time evolution with the solvable part $\hat{H}_0$ and a time-evolution operator $\hat{U}(t, t_0)$ (it is also called scattering operator $\hat{S}$ in some works). The time-evolution operator contains the perturbed Hamiltonian, and reads as $\hat{U}(t, t_0) = \hat{T} \exp[-i \int_{t_0}^t dt_1 \hat{H}_1(t_1)]$, where the time-ordering operator $\hat{T}$ is used to arrange the operators in the chronological order from the right to the left side. Making good use of the time-evolution operator $\hat{U}(t, t_0)$, we can obtain the real-time statistical average of an operator $\langle \hat{\mathcal{O}} \rangle_U = \mathrm{tr}[\hat{\rho}_0 \hat{\mathcal{O}} \hat{U}(t, t_0)]$, which also depends on an initial state.

In the above-mentioned treatment, we also have to introduce the Green's functions [71]. Generally, the Green's functions are defined as the average values of time-ordering operator products [72], which are shown as $\langle \hat{T}[\hat{a}_{j_1,U}^\dagger(t_1) \ldots \hat{a}_{j_n,U}(t_n)] \rangle_U$, where the notation j denotes the degree of freedom of the system, the whole subscript j_n, U represents that the annihilation operator of the nth degree of freedom, and $\hat{a}_{j_n,U}(t_n) = \hat{U}(t_0, t) \hat{a}_{j_n} \hat{U}(t, t_0)$ is translated from a Heisenberg picture to a Dirac (interaction) picture at an evolution time t_n. Correspondingly, the Dirac bracket $\langle \cdot \rangle_U$ denotes the real-time average value of the operator products with respect to the eigenstate of a system Hamiltonian. Obviously, we understand the operator $\hat{a}_{j_n,U}(t_n)$ and then know that each operator can carry out a forward and a backward time evolution. But due to the time-ordering operator $\hat{T}$, and based on the Gell-Mann-Low theorem, we can reduce the backward evolution, and simplify the expectation to the one of forward evolution along a straight time path. In this way, the perturbative treatment can be reduced to a series expansion of the time-evolution operator $\hat{U}(t, t_0)$. As a result, we can obtain the physical quantities which depend on some expectation values via a calculation of Green's functions [73]. For example, the energy spectrum of a quantum multiparticle system can be derived from the retarded Green's functions, and the lesser or greater Green's functions can determine the population $\mathcal{N}(t)$ and pumping rate $I_j(t)$ of particles, from which we have performed a calculation for the magnons in our work and display the derivation in the following.

In order to investigate more about the quantum features of the cavity optomagnonic system to confirm our result via numerical simulations, we theoretically calculate the pumping rate of the magnons in the polarization-state conversion. Based on the perturbative treatment, we can work out the derivation of the statistical expectation, where we do not have to obey the semiclassical approximation. To this end, we first divide the Hamiltonian in Eq. (A4) into the following two parts: (i) The first part is a local unperturbed part, with the form $\hat{H}_0 = -\Delta_H \hat{a}_H^\dagger \hat{a}_H - \Delta_V \hat{a}_V^\dagger \hat{a}_V - \Delta_m \hat{m}^\dagger \hat{m}$. (ii) The remaining part is the nonlocal perturbation, which reads as $\hat{H}_1 = -g\hat{a}_H^\dagger \hat{a}_V \hat{m}^\dagger - g\hat{a}_H \hat{a}_V^\dagger \hat{m}$. After this, we are interested in the pumping rate mentioned above, which is the change of magnon number per unit time in our work. It is

governed by

$$\frac{\partial}{\partial t} \Delta_m \hat{m}^\dagger \hat{m} = i \Delta_m g (\hat{a}_H^\dagger \hat{a}_V \hat{m}^\dagger + \hat{a}_H \hat{a}_V^\dagger \hat{m}) \qquad \text{(E1)}$$

in the framework rotating, which arises from the Heisenberg equation of motion $\frac{\partial}{\partial t} \hat{\mathcal{O}} = [\hat{\mathcal{O}}, \hat{H}]/i$. As described in the main text, the magnons create or annihilate together with the H-polarized photons. Thereby, we can treat the pumping rate of the magnons and the one of H-polarized photons as the coincidence. Then, by applying the Schwinger-Keldysh formalism on the cavity optomagnonic model to perturbatively evaluate the statistical average of operator product in the full quantum regime, and the pumping rate reads as

$$I_m(t) = 2\Delta_m g \, \mathrm{Im} \langle \hat{m}(t^+) \hat{a}_H \hat{a}_V^\dagger(t^-) \rangle_U, \qquad \text{(E2)}$$

where the superscripts "+" and "−" represent the forward and backward time evolution on the Keldysh contour. The real-time average inside the pumping rate $\langle \hat{\mathcal{O}} \rangle_U = \mathrm{tr}[\hat{\rho}_0 \hat{\mathcal{O}} \hat{U}(t, t_0)]$ is governed by the time-evolution operator $\hat{U}(t, t_0)$, which originates from the interaction Hamiltonian $\hat{H}_1$, with the above definition $\hat{U}(t, t_0) = \hat{T} \exp[-i \int_{t_0}^t dt_1 \hat{H}_1(t_1)]$. Subsequently, we make an expansion of the operator $\hat{U}$ up to the first order in the optomagnonic coupling constant g, which is much smaller than the other involved parameters. Then, we get the average value in the following:

$$\langle \hat{m}(t^+) \hat{a}_H \hat{a}_V^\dagger(t^-) \rangle_U$$
$$= ig \int \langle \hat{T} \hat{m}(t) \hat{m}^\dagger(t') \rangle_0 \langle \hat{T} \hat{a}_H^\dagger(t) \hat{a}_V(t) \hat{a}_H(t') \hat{a}_V^\dagger(t') \rangle_0 dt',$$
$$\text{(E3)}$$

where the subscript "0" means the average value of an operator at the initial state $\langle \hat{\mathcal{O}} \rangle_0 = \mathrm{tr}(\hat{\rho}_0 \hat{\mathcal{O}})$. Under the Langreth rule, we can associate the nonequilibrium Green's functions with the real-time Green's functions, and achieve the expression of the real-time pumping rate as

$$I_m(t) = 2\Delta_m g^2 \mathrm{Re} \int F_{t,t'}^{\mathcal{R}} G_{t',t}^< + F_{t,t'}^< G_{t',t}^{\mathcal{R}} dt', \qquad \text{(E4)}$$

where the nonequilibrium Green's functions under the integral in Eq. (E3) are well defined by

$$iF_{t,t'} = \langle \hat{T} \hat{m}(t) \hat{m}^\dagger(t') \rangle_0, \qquad \text{(E5a)}$$

$$iG_{t,t'} = \langle \hat{T} \hat{a}_H^\dagger(t) \hat{a}_V(t) \hat{a}_H(t') \hat{a}_V^\dagger(t') \rangle_0 \qquad \text{(E5b)}$$

for the magnonic and polarized optical subsystem, respectively. The subscript of Green's functions t, t' means that the forward time evolution starts at an initial time, then it excurses a time t' and finally finishes at a time t. The components of the Green's functions are defined by

$$iF_{t,t'}^< = -\langle \hat{m}^\dagger(t') \hat{m}(t) \rangle_0, \qquad \text{(E6a)}$$

$$iF_{t,t'}^> = \langle \hat{m}(t) \hat{m}^\dagger(t') \rangle_0, \qquad \text{(E6b)}$$

$$iF_{t,t'}^{\mathcal{R}} = i\theta(t - t')(F_{t,t'}^> - F_{t,t'}^<), \qquad \text{(E6c)}$$

$$iG_{t,t'}^< = -\langle \hat{a}_H(t') \hat{a}_V^\dagger(t') \hat{a}_H^\dagger(t) \hat{a}_V(t) \rangle_0, \qquad \text{(E6d)}$$

$$iG_{t,t'}^> = \langle \hat{a}_H^\dagger(t) \hat{a}_V(t) \hat{a}_H(t') \hat{a}_V^\dagger(t') \rangle_0, \qquad \text{(E6e)}$$

$$iG_{t,t'}^{\mathcal{R}} = i\theta(t - t')(G_{t,t'}^> - G_{t,t'}^<). \qquad \text{(E6f)}$$

The superscripts "<" and ">" represent the normal order and antinormal order products of the magnonic operators in Eqs. (E6a)–(E6b), corresponding to the lesser and greater components of the Green's functions. And $G_{t,t'}^{\mathcal{R}}$ in Eq. (E6c) is the retarded Green's function. In Eqs. (E6d)–(E6f), there is a similar definition of the lesser, greater, and retarded Green's functions for the optical subsystem. Furthermore, the optical subsystem is constituted of two modes, i.e., the H- and V-polarized photonic modes. As a result, the nonequilibrium Green's function of the optical subsystem can be written as a concise form

$$G_{t,t'} = i\langle \hat{T} \hat{a}_H^\dagger(t)\hat{a}_V(t)\hat{a}_H(t')\hat{a}_V^\dagger(t')\rangle_0$$
$$= i\langle \hat{T} \hat{a}_H^\dagger(t)\hat{a}_H(t')\rangle_0 \langle \hat{T} \hat{a}_V(t)\hat{a}_V^\dagger(t')\rangle_0. \quad \text{(E7)}$$

Then we take above Green's functions apart to two series of functions for the subsystems of H- and V-polarized photons, the lesser component is shown by

$$iG_{t,t'}^< = -\langle \hat{a}_H(t')\hat{a}_H^\dagger(t)\rangle_0 \langle \hat{a}_V^\dagger(t')\hat{a}_V(t)\rangle_0 \equiv G_{H;t',t}^> G_{V;t,t'}^>. \quad \text{(E8)}$$

And the greater component is shown by

$$iG_{t,t'}^> = \langle \hat{a}_H^\dagger(t)\hat{a}_H(t')\rangle_0 \langle \hat{a}_V(t)\hat{a}_V^\dagger(t')\rangle_0 \equiv -G_{H;t',t}^> G_{V;t,t'}^<. \quad \text{(E9)}$$

Therefore, the retarded component $G_{t,t'}^{\mathcal{R}}$ can be decomposed to

$$G_{t,t'}^{\mathcal{R}} = i\theta(t-t')(G_{H;t',t}^> G_{V;t,t'}^< + G_{H;t',t}^< G_{V;t,t'}^>). \quad \text{(E10)}$$

In order to solve out this retarded Green's function, we explicitly write the lesser and greater components for each optical mode as

$$G_{j;t,t'}^< = \langle \hat{a}_j^\dagger(t')\hat{a}_j(t)\rangle_0 = \langle \hat{a}_j^\dagger \hat{a}_j\rangle_0 e^{-i\Delta_j(t-t')}, \quad \text{(E11a)}$$

$$G_{j;t,t'}^> = \langle \hat{a}_j^\dagger(t)\hat{a}_j(t')\rangle_0 = \langle \hat{a}_j^\dagger \hat{a}_j\rangle_0 e^{-i\Delta_j(t-t')}. \quad \text{(E11b)}$$

After this, the retarded component in the time domain can be obtained as

$$iG_{t,t'}^R = \theta(t-t') \times \{2\langle \hat{a}_H^\dagger \hat{a}_H\rangle_0 \langle \hat{a}_V^\dagger \hat{a}_V\rangle_0$$
$$+ \langle \hat{a}_H^\dagger \hat{a}_H + \hat{a}_H^\dagger \hat{a}_H\rangle_0\} e^{-i\Delta_m(t-t')}$$
$$= \theta(t-t')(2\mathcal{N}_{H,0}\mathcal{N}_{V,0} + \mathcal{N}_0)e^{-i\Delta_m(t-t')}, \quad \text{(E12)}$$

where $\mathcal{N}_{H,0}$ and $\mathcal{N}_{V,0}$ are the photon number at the H- and V-polarized state at the initial time, and $\mathcal{N}_0$ is the total photon number of both optical modes at the initial state. Here we use the triple-resonance condition $\Delta_V - \Delta_H - \Delta_m = 0$. Then applying the Fourier transformation, we can derive the retarded Green's function in the frequency domain

$$G_\omega^R = \frac{2\mathcal{N}_{H,0}\mathcal{N}_{V,0} + \mathcal{N}_0}{\Delta - \Delta_m + i\kappa_c/2}. \quad \text{(E13)}$$

Similarly, the retarded Green's function for the magnonic subsystem can be obtained as

$$F_\omega^R = \frac{1}{\Delta_m + i\kappa_m/2}. \quad \text{(E14)}$$

Finally, by making use of the nonequilibrium distribution difference [74]

$$\delta f_\omega = \frac{F_\omega^<}{2i\,\text{Im}F_\omega^R} - \frac{G_\omega^<}{2i\,\text{Im}G_\omega^R}, \quad \text{(E15)}$$

we can make the integral in Eq. (E4) simpler. As a result, the pumping rate in the steady-state limit can be written as

$$I_m^{ss} = 4\omega_m g^2 \text{Im}\frac{1}{\Delta_m + i\kappa_m/2}\text{Im}\frac{2\mathcal{N}_{H,0}\mathcal{N}_{V,0} + \mathcal{N}_0}{\Delta - \Delta_m + i\kappa_c/2}, \quad \text{(E16)}$$

which is determined by the initial state of the cavity optomagnonic system and the detunings of the driving fields.

From the above results via the Schwinger-Keldysh theory, we easily find that when the driving fields of the cavity optomagnonic system fulfill the magnonic resonance condition $\Delta_m = 0$, in the meanwhile optical resonance $\Delta = 0$ is also satisfied, the pumping rate of the magnons (also the photons) can reach the maximum. It also means that the quantum state conversion between the H- and V-polarized states can work most drastically on the magnonic resonance $\Delta_m = 0$, which matches the numerical simulations in the main text and confirms our work. These achievable results based on the perturbative calculations can help in further understanding the quantum features in the cavity optomagnonic model.

[1] D. D. Stancil and A. Prabhakar, *Spin Waves: Theory and Applications* (Springer, Boston, 2009).

[2] A. Borovik-Romanov and S. Sinha, *Spin Waves and Magnetic Excitations* (Elsevier, Amsterdam, 1988), Vol. 22, pp. 88–100.

[3] S. V. Kusminskiy, *Cavity Optomagnonics*, Springer Briefs in Physics (Springer, Cham, 2019), pp. 45–59.

[4] P. A. Pantazopoulos, N. Stefanou, E. Almpanis, and N. Papanikolaou, Photomagnonic nanocavities for strong light–spin-wave interaction, Phys. Rev. B **96**, 104425 (2017).

[5] S. V. Kusminskiy, Cavity Optomagnonics, in *Opto- magnonic Structures: Novel Architectures for Simultaneous Control of Light and Spin Waves* (World Scientific, Singapore, 2021), pp. 299–353.

[6] B. Z. Rameshti, S. V. Kusminskiy, J. A. Haigh, K. Usami, D. Lachance-Quirion, Y. Nakamura, C.-M. Hu, H. X. Tang, G. E. W. Bauer, Y. M. Blanter, Cavity magnonics, Phys. Rep. **979**, 1 (2022).

[7] Y. Tabuchi, S. Ishino, A. Noguchi, T. Ishikawa, R. Yamazaki, K. Usami, and Y. Nakamura, Coherent coupling between a ferromagnetic magnon and a superconducting qubit, Science **349**, 405 (2015).

[8] I. A. Golovchanskiy, N. N. Abramov, V. S. Stolyarov, M. Weides, V. V. Ryazanov, A. A. Golubov, A. V. Ustinov, and M. Y. Kupriyanov, Ultrastrong photon-to-magnon coupling in multilayered heterostructures involving superconducting coherence via ferromagnetic layers, Sci. Adv. **7**, eabe8638 (2021).

[9] Y. Tabuchi, S. Ishino, T. Ishikawa, R. Yamazaki, K. Usami, and Y. Nakamura, Hybridizing Ferromagnetic Magnons and Microwave Photons in the Quantum Limit, Phys. Rev. Lett. **113**, 083603 (2014).

[10] X. Zhang, C.-L. Zou, L. Jiang, and H. X. Tang, Strongly Coupled Magnons and Cavity Microwave Photons, Phys. Rev. Lett. **113**, 156401 (2014).

[11] M. Harder, Y. Yang, B. M. Yao, C. H. Yu, J. W. Rao, Y. S. Gui, R. L. Stamps, and C. M. Hu, Level Attraction Due to Dissipative Magnon-Photon Coupling, Phys. Rev. Lett. **121**, 137203 (2018).

[12] Y. Yang, Y. P. Wang, J. W. Rao, Y. S. Gui, B. M. Yao, W. Lu, and C. M. Hu, Unconventional Singularity in Anti-Parity-Time Symmetric Cavity Magnonics, Phys. Rev. Lett. **125**, 147202 (2020).

[13] F.-X. Sun, S.-S. Zheng, Y. Xiao, Q. Gong, Q. He, and K. Xia, Remote Generation of Magnon Schrödinger Cat State via Magnon-Photon Entanglement, Phys. Rev. Lett. **127**, 087203 (2021).

[14] H. Man, Z. Shi, G. Xu, Y. Xu, X. Chen, S. Sullivan, J. Zhou, K. Xia, J. Shi, P. Dai, Direct observation of magnon-phonon coupling in yttrium iron garnet, Phys. Rev. B **96**, 100406(R) (2017).

[15] M. Asjad, J. Li, S.-Y. Zhu and J. Q. You, Magnon squeezing enhanced ground-state cooling in cavity magnomechanics, Fund. Res. **3**, 3 (2023).

[16] D. Zhang, X.-Q. Luo, Y.-P. Wang, T.-F. Li, and J. Q. You, Observation of the exceptional point in cavity magnon-polaritons, Nat. Commun. **8**, 1368 (2017).

[17] Y. P. Wang, G. Q. Zhang, D. Zhang, T. F. Li, C. M. Hu, and J. Q. You, Bistability of Cavity Magnon Polaritons, Phys. Rev. Lett. **120**, 057202 (2018).

[18] C. Zhao, X. Li, S. Chao, R. Peng, C. Li, and L. Zhou, Simultaneous blockade of a photon, phonon, and magnon induced by a two-level atom, Phys. Rev. A **101**, 063838 (2020).

[19] J. Zhao, Y. Liu, L. Wu, C.-K. Duan, Y.-X. Liu, and J. Du, Observation of Anti-$\mathcal{PT}$-Symmetry Phase Transition in the Magnon-Cavity-Magnon Coupled System, Phys. Rev. Appl. **13**, 014053 (2020).

[20] J. A. Haigh, S. Langenfeld, N. J. Lambert, J. J. Baumberg, A. J. Ramsay, A. Nunnenkamp, and A. J. Ferguson, Magneto-optical coupling in whispering-gallery-mode resonators, Phys. Rev. A **92**, 063845 (2015).

[21] E. Almpanis, G. P. Zouros, P. A. Pantazopoulos, K. L. Tsakmakidis, N. Papanikolaou, and N. Stefanou, Spherical optomagnonic microresonators: Triple-resonant photon transitions between Zeeman-split Mie modes, Phys. Rev. B **101**, 054412 (2020).

[22] A. Osada, R. Hisatomi, A. Noguchi, Y. Tabuchi, R. Yamazaki, K. Usami, M. Sadgove, R. Yalla, M. Nomura, Y. Nakamura, Cavity Optomagnonics with Spin-Orbit Coupled Photons, Phys. Rev. Lett. **116**, 223601 (2016).

[23] S. V. Kusminskiy, H. X. Tang, and F. Marquardt, Coupled spin-light dynamics in cavity optomagnonics, Phys. Rev. A **94**, 033821 (2016).

[24] X. Zhang, N. Zhu, C. L. Zou, and H. X. Tang, Optomagnonic Whispering Gallery Microresonators, Phys. Rev. Lett. **117**, 123605 (2016).

[25] J. A. Haigh, A. Nunnenkamp, A. J. Ramsay, and A. J. Ferguson, Triple-Resonant Brillouin Light Scattering in Magneto-Optical Cavities, Phys. Rev. Lett. **117**, 133602 (2016).

[26] S. Sharma, Y. M. Blanter, and G. E. W. Bauer, Light scattering by magnons in whispering gallery mode cavities, Phys. Rev. B **96**, 094412 (2017).

[27] R. Hisatomi, A. Noguchi, R. Yamazaki, Y. Nakata, A. Gloppe, Y. Nakamura, and K. Usami, Helicity-Changing Brillouin Light Scattering by Magnons in a Ferromagnetic Crystal, Phys. Rev. Lett. **123**, 207401 (2019).

[28] S. Sharma, Y. M. Blanter, and G. E. W. Bauer, Optical Cooling of Magnons, Phys. Rev. Lett. **121**, 087205 (2018).

[29] J. A. Haigh, A. Nunnenkamp, and A. J. Ramsay, Polarization Dependent Scattering in Cavity Optomagnonics, Phys. Rev. Lett. **127**, 143601 (2021).

[30] Z.-X. Liu and H. Xiong, Magnon laser based on Brillouin light scattering, Opt. Lett. **45**, 5452 (2020).

[31] Y.-J. Xu and J. Song, Nonreciprocal magnon laser, Opt. Lett. **46**, 5276 (2021).

[32] S. Dufferwiel, F. Li, E. Cancellieri, L. Giriunas, A. A. P. Trichet, D. M. Whittaker, P. M. Walker, F. Fras, E. Clarke, J. M. Smith, M. S. Skolnick, and D. N. Krizhanovskii, Spin Textures of Exciton-Polaritons in a Tunable Microcavity with Large TE-TM Splitting, Phys. Rev. Lett. **115**, 246401 (2015).

[33] I. Gnusov, H. Sigurdsson, J. D. Töpfer, S. Baryshev, S. Alyatkin, and P. G. Lagoudakis, All-Optical Linear-Polarization Engineering in Single and Coupled Exciton-Polariton Condensates, Phys. Rev. Appl. **16**, 034014 (2021).

[34] S. Baryshev, A. Zasedatelev, H. Sigurdsson, I. Gnusov, J. D. Töpfer, A. Askitopoulos, and P. G. Lagoudakis, Engineering Photon Statistics in a Spinor Polariton Condensate, Phys. Rev. Lett. **128**, 087402 (2022).

[35] C. Dong, V. Fiore, M. C. Kuzyk, and H. Wang, Optomechanical Dark Mode, Science **338**, 1609 (2012).

[36] J. T. Hill, A. H. Safavi-Naeini, J. Chan, and O. Painter, Coherent optical wavelength conversion via cavity optomechanics, Nat. Commun. **3**, 1196 (2012).

[37] H. Xiong, Y.-M. Huang, L.-L. Wan, and Y. Wu, Vector cavity optomechanics in the parameter configuration of optomechanically induced transparency, Phys. Rev. A **94**, 013816 (2016).

[38] R. Duggan, J. del Pino, E. Verhagen, and A. Alù, Optomechanically Induced Birefringence and Optomechanically Induced Faraday Effect, Phys. Rev. Lett. **123**, 023602 (2019).

[39] S. Wielandy and A. L. Gaeta, Phys. Coherent Control of the Polarization of an Optical Field, Phys. Rev. Lett. **81**, 3359 (1998).

[40] A. S. Parkins and H. J. Kimble, Quantum state transfer between motion and light, J. Opt. B: Quantum Semiclass. Opt. **1**, 496 (1999).

[41] L. Tian, Adiabatic State Conversion and Pulse Transmission in Optomechanical Systems, Phys. Rev. Lett. **108**, 153604 (2012).

[42] Y.-D. Wang and A. A. Clerk, Using Interference for High Fidelity Quantum State Transfer in Optomechanics, Phys. Rev. Lett. **108**, 153603 (2012).

[43] M.-A. Miri, F. Ruesink, E. Verhagen, and A. Alù, Optical Nonreciprocity Based on Optomechanical Coupling, Phys. Rev. Appl. **7**, 064014 (2017).

[44] C. Genes, A. Mari, P. Tombesi, and D. Vitali, Robust entanglement of a micromechanical resonator with output optical fields, Phys. Rev. A **78**, 032316 (2008).

[45] L. Tian and H. Wang, Optical wavelength conversion of quantum states with optomechanics, Phys. Rev. A **82**, 053806 (2010).

[46] Y. Benny, S. Khatsevich, Y. Kodriano, E. Poem, R. Presman, D. Galushko, P. M. Petroff, and D. Gershoni, Coherent Optical Writing and Reading of the Exciton Spin State in Single Quantum Dots, Phys. Rev. Lett. **106**, 040504 (2011).

[47] C. Antón, P. Hilaire, C. A. Kessler, J. Demory, C. Gómez, A. Lemaître, I. Sagnes, N. D. Lanzillotti-Kimura, O. Krebs, N. Somaschi, P. Senellart, and L. Lanco, Tomography of the optical polarization rotation induced by a single quantum dot in a cavity, Optica **4**, 1326 (2017).

[48] Q. A. Turchette, C. J. Hood, W. Lange, H. Mabuchi, and H. J. Kimble, Measurement of Conditional Phase Shifts for Quantum Logic, Phys. Rev. Lett. **75**, 4710 (1995).

[49] J. R. Sandercock, W. Wettling, *Light Scattering from Thermal Acoustic Magnons in Yttrium Iron Garnet* (Pergamon, Oxford, 1973), Vol. 13, pp. 1729–1732.

[50] W. Wettling, *Magnetooptical Properties of YIG Measured on a Continuously Working Spectrometer* (Springer, Berlin, 1975), Vol. 6, pp. 367–372.

[51] W. Wettling, M. G. Cottam, and J. R. Sandercock, The relation between one-magnon light scattering and the complex magneto-optic effects in YIG, J. Phys. C: Solid State Phys. **8**, 211 (1975).

[52] W. Wettling, *Magneto-optics of Ferrites* (North-Holland, Amsterdam, 1976), Vol. 3, pp. 147–160.

[53] V. A. S. V. Bittencourt, I. Liberal, and S. V. Kusminskiy, Light propagation and magnon-photon coupling in optically dispersive magnetic media, Phys. Rev. B **105**, 014409 (2022).

[54] V. A. S. V. Bittencourt, I. Liberal, and S. V. Kusminskiy, Optomagnonics in Dispersive Media: Magnon-Photon Coupling Enhancement at the Epsilon-near-Zero Frequency, Phys. Rev. Lett. **128**, 183603 (2022).

[55] M.-O. Pleinert, J. von Zanthier, and G. S. Agarwal, Phase control of the quantum statistics of collective emission, Phys. Rev. A **97**, 023831 (2018).

[56] Q.-U.-A. Gulfam and Z. Ficek, Highly directional photon superbunching from a few-atom chain of emitters, Phys. Rev. A **98**, 063824 (2018).

[57] H. J. Carmichael, *Statistical Methods in Quantum Optics* 1, 2nd ed. (Springer, Berlin, 2002).

[58] G. S. Agarwal, *Quantum Optics* (Cambridge University Press, Cambridge, UK, 2013).

[59] C. W. Gardiner and P. Zoller, *Quantum Noise: A Handbook of Markovian and Non-Markovian Quantum Stochastic Methods with Applications to Quantum Optics*, 3rd ed., Springer Series in Synergetics (Springer, Berlin, 2004).

[60] M. Aspelmeyer, T. J. Kippenberg, and F. Marquardt, Cavity optomechanics, Rev. Mod. Phys. **86**, 1391 (2014).

[61] M. Cai, O. Painter, and K. J. Vahala, Observation of Critical Coupling in a Fiber Taper to a Silica-Microsphere Whispering-Gallery Mode System, Phys. Rev. Lett. **85**, 74 (2000).

[62] S. Weis, R. Riviere, S. Deleglise, E. Gavartin, O. Arcizet, A. Schliesser, and T. J. Kippenberg, Optomechanically induced transparency, Science **330**, 1520 (2010).

[63] G.-Q. Zhang, Z. Chen, D. Xu, N. Shammah, M. Liao, T.-F. Li, L. Tong, S.-Y. Zhu, F. Nori, and J. Q. You, Exceptional point and cross-relaxation effect in a hybrid quantum system, PRX Quantum **2**, 020307 (2021).

[64] J. D. Jackson, *Classical Electrodynamics*, 3rd ed. (Wiley, New York, 1998).

[65] Z. Shen, Y.-L. Zhang, Y. Chen, C.-L. Zou, Y.-F. Xiao, X.-B. Zou, F.-W. Sun, G.-C. Guo, and C.-H. Dong, Experimental realization of optomechanically induced non-reciprocity, Nat. Photonics **10**, 657 (2016).

[66] R. Huang, A. Miranowicz, J.-Q. Liao, F. Nori, and H. Jing, Nonreciprocal Photon Blockade, Phys. Rev. Lett. **121**, 153601 (2018).

[67] H. Zhang, R. Huang, S.-D. Zhang, Y. Li, C.-W. Qiu, F. Nori, and H. Jing, Breaking anti-pt symmetry by spinning a resonator, Nano Lett. **20**, 7594 (2020).

[68] X. Xu, Y. Zhao, H. Wang, H. Jing, and A. Chen, Quantum nonreciprocality in quadratic optomechanics, Photon. Res. **8**, 143 (2020).

[69] C. W. Gardiner and M. J. Collett, Input and output in damped quantum systems: Quantum stochastic differential equations and the master equation, Phys. Rev. A **31**, 3761 (1985).

[70] T. D. Graß, F. E. A. dos Santos, and A. Pelster, Excitation spectra of bosons in optical lattices from the Schwinger-Keldysh calculation, Phys. Rev. A **84**, 013613 (2011).

[71] A.-P. Jauho, N. S. Wingreen, and Y. Meir, Time-dependent transport in interacting and noninteracting resonant-tunneling systems, Phys. Rev. B **50**, 5528 (1994).

[72] G. D. Mahan, *Many-Particle Physics* (Plenum, New York, 1990).

[73] S. Datta, *Electronic Transport in Mesoscopic Systems* (Cambridge University Press, New York, 1995).

[74] D. Oue and M. Matsuo, Twisting an optomechanical cavity, Phys. Rev. A **106**, L041501 (2022).